Published in final edited form as:

Dev Cell. 2023 October 23; 58(20): 2080–2096.e7. doi:10.1016/j.devcel.2023.07.011.

Rejection of inappropriate synaptic partners in mouse retina mediated by transcellular FLRT2-UNC5 signaling

Cameron L. Prigge[1,4], **Mayur Dembla**[*,1], **Arsha Sharma**[*,1], **Malak El-Quessny**[2], **Christopher Kozlowski**[1], **Caitlin E. Paisley**[1], **Adam M. Miltner**[1], **Tyler M. Johnson**[1], **Luca Della Santina**[3], **Marla B. Feller**[2], **Jeremy N. Kay**[1,#]

[1]Departments of Neurobiology, Ophthalmology, and Cell Biology, Duke University School of Medicine, Box 3802, Durham, NC 27710 USA.

[2]Helen Wills Neuroscience Institute and Department of Molecular and Cell Biology, University of California, Berkeley, Berkeley, CA 94720 USA.

[3]Department of Vision Sciences, University of Houston College of Optometry. Houston, TX 77204 USA

[4]Present address: Department of Physiology, Neuroscience Program, Michigan State University, East Lansing, MI 48824 USA.

SUMMARY

During nervous system development, neurons choose synaptic partners with remarkable specificity; however, the cell-cell recognition mechanisms governing rejection of inappropriate partners remain enigmatic. Here we show that mouse retinal neurons avoid inappropriate partners using the FLRT2-UNC5 receptor-ligand system. Within the inner plexiform layer (IPL), FLRT2 is expressed by direction-selective (DS) circuit neurons, whereas UNC5C/D are expressed by non-DS neurons projecting to adjacent IPL sublayers. In vivo gain- and loss-of-function experiments demonstrate that FLRT2-UNC5 binding eliminates growing DS dendrites that have strayed from the DS circuit IPL sublayers. Abrogation of FLRT2-UNC5 binding allows mistargeted arbors to persist, elaborate, and acquire synapses from inappropriate partners. Conversely, UNC5C misexpression within DS circuit sublayers inhibits dendrite growth and drives arbors into adjacent sublayers. Mechanistically, UNC5s promote dendrite elimination by interfering with FLRT2-

---

Correspondence to: jeremy.kay@duke.edu.

[*]Equal contribution

[#]lead contact

AUTHOR CONTRIBUTIONS
Conceptualization: C.L.P. and J.N.K. Methodology: C.L.P., M.D., M.E-Q., and C.E.P. Experiments and data analysis: C.L.P., A.S, M.D., C.K., M.E-Q., A.M.M., and T.J. Software: L.D.S. Writing original draft: C.L.P. and J.N.K. Writing - review and editing: C.L.P., M.D., C.K., C.E.P., M.B.F. Visualization: C.L.P., M.D., and J.N.K. Supervision: M.B.F. and J.N.K. Project administration: J.N.K. Funding acquisition: C.L.P., M.E-Q., L.D.S., J.N.K.

DECLARATION OF INTERESTS
The authors declare no competing interests.

mediated adhesion. Based on their broad expression, FLRT-UNC5 recognition is poised to exert widespread effects upon synaptic partner choices across the nervous system.

Graphical Abstract

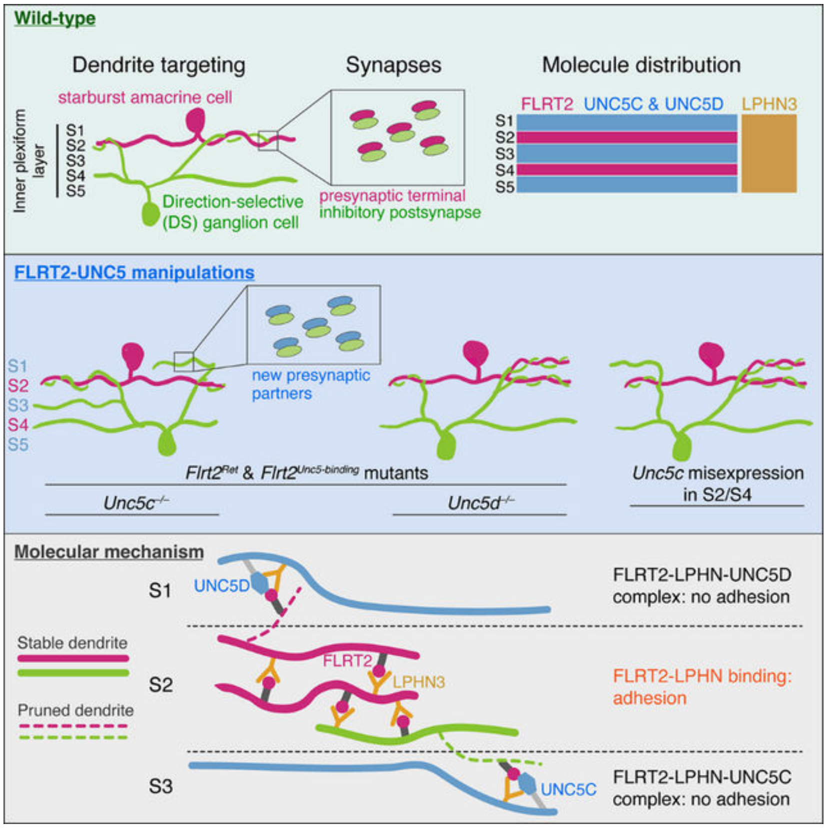

eTOC Blurb

Precise assembly of neural circuits depends on the ability of developing neurons to shun inappropriate synaptic partners. Prigge et al. show that transcellular binding between FLRT2 and its UNC5-family ligands prevents FLRT2$^+$ dendrites from adhering to inappropriate partners, thereby enforcing precise wiring of a retinal motion-sensitive circuit.

INTRODUCTION

During nervous system development, growing neurons actively choose which cells to connect with and which to avoid using cell-surface receptors. These synaptic choices establish neural circuits dedicated to specific computations and functions. Synaptogenic defects can compromise circuit function; but despite their importance, the molecular mechanisms underlying synaptic partner choices remain enigmatic[1].

Molecular studies of synaptic specificity have mainly focused on positive cues, such as attractive or adhesive recognition molecules, that affirm appropriate connections. By contrast, far less is known about negative cues, which discourage inappropriate connections[1–3]. It is generally presumed that negative cues have important roles in wiring specificity, but few clear-cut examples are currently known[4]. Most negative cues identified so far are repulsive guidance molecules that prevent axons and dendrites from growing into particular regions[1,3,5–7]. In many cases, deletion of such guidance molecules can alter neurite targeting without disturbing the correct pairing of synaptic partners[8,9]. Therefore, negative cues that are centrally involved in partner selection remain to be discovered.

The mouse retina is a useful model system to investigate synaptic partner choice, due to the stereotyped laminar organization of synapses within the inner plexiform layer (IPL; Fig. 1A). This laminar organization facilitates the cellular rendezvous necessary for circuit-specific wiring. To examine how negative cues establish laminar and synaptic specificity, we used the mouse retinal direction-selective (DS) circuit (Fig. 1A) as our model system. This evolutionarily conserved circuit encodes the direction of image motion through spiking activity of direction-selective retinal ganglion cells (DSGCs), thereby driving multiple visual behaviors[10–16]. The DS circuit occupies two dedicated IPL sublayers, denoted S2 and S4, which respectively encode light OFF or ON responses (Fig. 1A). Within these sublayers, dendrites of ON-OFF (oo)DSGCs receive input from presynaptic circuit partners, including 1) glutamatergic bipolar cells; and 2) starburst amacrine cells, which provide extensive GABAergic inhibitory inputs that are a crucial determinant of the DS computation[12,17–20]. Strict dendritic co-stratification within S2 and S4 (Fig. 1A) ensures that the vast majority of inhibitory inputs onto ooDSGC dendrites are supplied by starburst amacrine cells[21–24]. Numerous other amacrine cell types project to IPL sublayers directly adjacent to the DS circuit, mere microns away, and would therefore be easily accessible to ooDSGC dendrites during synaptogenesis. Nevertheless, ooDSGCs avoid such connections. The mechanisms that prevent ooDSGCs from forming synapses in adjacent non-DS layers remain unknown.

Previous studies of DS circuit synaptic specificity identified positive cues that bring DS circuit partners together within the IPL. This process starts around postnatal day (P) 0 in mice, when starbursts use homotypic recognition mechanisms to stratify their arbors into two IPL sublayers[25,26]. Then, between P0 and P6, adhesion molecules recruit ooDSGC dendrites and bipolar cell axons to the starburst laminar scaffold[27–29]. In principle, these affirmative cues could suffice to dictate laminar and synaptic specificity. However, our past work suggests that negative cues may also be positioned to drive specificity by preventing DS circuit arbors from entering adjacent non-DS sublayers[30]. We studied fibronectin leucine-rich repeat transmembrane (FLRT) proteins, a multifunctional family of cell-surface molecules that participate in adhesion, repulsion, and synaptogenesis[31]. These effects are mediated by binding to multiple ligands, including those of the Uncoordinated-5 (UNC5) family[30,32–35]. We previously showed that FLRT2 and UNC5C are a repulsive receptor-ligand pair that is expressed in complementary patterns within the developing IPL. FLRT2 is expressed by starburst and ooDSGC neurons and localizes to DS circuit IPL sublayers; UNC5C, meanwhile, fills surrounding IPL strata[30] (see schematic, Fig. 1D,E). Another FLRT2 ligand, UNC5D, shares a similar expression pattern with UNC5C[30]. In stripe assays using cultured primary retinal neurons, UNC5C inhibits arbor growth by FLRT2$^+$ cells, including starburst amacrine cells and ooDSGCs[30]. These results suggest that FLRT2-UNC5 interactions could prevent starburst and ooDSGC dendrites from straying into adjacent IPL regions, although this idea remains to be tested in vivo.

In this study we sought to answer two major questions. First, does FLRT2-UNC5 signaling impact DS circuit laminar specificity in vivo? We addressed this issue by focusing on DS circuit cell types that express FLRT2 – the starburst amacrine cells and ooDSGCs[30] – which we refer to collectively here as "DS circuit neurons." Second, we asked how FLRT2-UNC5 signaling repels growing dendrites. We previously proposed a bidirectional "repellent receptor" model for laminar segregation, whereby FLRT2 and UNC5C both transduce repulsive guidance signals within their respective cell types upon binding to each other[30]. However, an alternative molecular model has since emerged from studies showing that FLRT2 has another key family of ligands, the latrophilins (LPHNs), and that FLRTs can simultaneously bind both ligands to form a tripartite complex[32,34,36–38]. FLRT-LPHN binding mediates adhesive and synaptogenic functions[34,39,40]; by contrast, the role of UNC5s in this complex remains uncertain. One study proposed that UNC5 binding interferes with FLRT-LPHN adhesion[32]. If this is true, UNC5s could control laminar targeting of FLRT2$^+$ neurons by inhibiting their adhesion to LPHN substrates. Therefore, we aimed to determine whether UNC5C guides FLRT2$^+$ arbors by a repellent receptor mechanism, as originally proposed[30], or by diminishing FLRT-mediated adhesion.

To address these questions we have deployed a wide range of mouse genetic tools to selectively disrupt FLRT2-UNC5 binding. We find that the FLRT2-UNC5 system enforces DS circuit laminar and synaptic specificity in vivo. Unexpectedly, this system serves as an error correction mechanism during a previously unappreciated developmental epoch when arbors of DS circuit neurons stray from the starburst scaffold. Finally, we show that UNC5 binding constrains growth of exuberant FLRT2$^+$ arbors by interfering with FLRT2-LPHN adhesion. Altogether, our results support a model in which affirmative mechanisms control the initial pairing of ooDSGC and starburst dendrites, whereas negative mechanisms – mediated by FLRT2-UNC5 binding – act during subsequent dendrite growth to prevent ooDSGC arbors from abandoning their synaptic partners.

RESULTS

Repulsion between adjacent circuits establishes DS circuit-specific IPL territories

The IPL expression patterns of FLRT2 and UNC5C proteins (Fig. 1D,E) led us to hypothesize that repulsion occurs between FLRT2$^+$ DS circuit arbors and UNC5C$^+$ arbors within adjacent sublayers. If this is true, there must exist a population of UNC5C-expressing neurons that exhibits mutual repulsion with the DS circuit. To identify such neurons we focused on the amacrine subtype marked by expression of glutamic acid decarboxylase-65 (GAD65). This amacrine population, which does not include starburst cells[41] (Supplemental Fig. S1F), drew our attention because of the mutually exclusive IPL labeling pattern we observed in tissue double-stained for GAD65 and starburst dendrite markers (vesicular acetylcholine transporter, VAChT; or choline acetyltransferase, ChAT; Fig. 1B). These sharp boundaries suggested that repulsion may occur between DS circuit and GAD65$^+$ arbors.

To test whether repulsion in fact occurs, we altered DS circuit laminar targeting and evaluated the effects upon GAD65$^+$ IPL projections. To this end we leveraged a mouse mutant that perturbs laminar targeting of starburst neurons in a cell-autonomous fashion. We previously showed that *Megf10* mutants exhibit focal disruptions in starburst and ooDSGC laminar targeting involving both gaps in IPL innervation and displacement of arbors into ectopic sublayers[26]. If DS circuit and GAD65$^+$ arbors repel each other, shifting the IPL location of DS circuit arbors should produce corresponding changes in GAD65 arbors. Consistent with this prediction, mistargeted starburst arbors that entered GAD65 territory did not commingle with GAD65$^+$ arbors, instead displacing them from their IPL strata (Fig. 1B,C). Furthermore, gaps in DS circuit IPL sublayers were inappropriately innervated by GAD65$^+$ arbors, suggesting a defect in repulsion when starburst and/or ooDSGC arbors are absent (Fig. 1B,C). All mutants analyzed (n = 4) showed both types of GAD65 projection errors. These results indicate that repulsive cues prevent DS circuit and GAD65$^+$ IPL sublayers from intermingling.

To investigate whether UNC5C could be involved in this repulsion, we next tested for expression of UNC5C by GAD65$^+$ amacrine cells. In situ hybridization for *Unc5c* and *Gad2* – the gene encoding GAD65 – revealed that *Unc5c* labels a subset of Gad65$^+$ amacrine cells at P6 and P15 (Fig. 1F,G; Supplemental Fig. S1A). While *Unc5c* also labeled other cell types, such as retinal ganglion cells (RGCs), most *Unc5c*$^+$ amacrine cells were Gad65$^+$ (Fig. 1F–H; Supplemental Fig. S1). This finding is consistent with the notable laminar overlap between GAD65$^+$ and UNC5C$^+$ arbors in the IPL (Fig 1B,E). We confirmed the Gad65$^+$ identity of *Unc5c*$^+$ amacrine cells using single-cell RNA-sequencing data[42] and by immunostaining primary retinal neurons in culture (n = 19/19 UNC5C$^+$ cells expressed GAD65; Supplemental Fig. S1B–E). Altogether, these results demonstrate that UNC5C is expressed by a specific GABAergic amacrine subpopulation that exhibits mutual repulsion with FLRT2$^+$ DS circuit IPL arbors. Therefore, this receptor-ligand pair is positioned to provide repulsive laminar targeting cues during DS circuit development.

DS circuit laminar targeting errors in *Flrt2* mutant mice

To test whether FLRT2-UNC5C signaling is required for DS circuit laminar targeting, we used a variety of genetic approaches to disrupt this interaction and then assessed whether starburst or ooDSGC dendritic arbors stray from their normal S2 and S4 sublayers. First, we generated retina-specific *Flrt2* mutants (denoted *Flrt2*^{Ret}), in which *Six3-Cre*[43] drives retinal recombination of a *Flrt2*^{flox} allele. Antibody labeling verified that FLRT2 protein was absent from retinas of *Flrt2*^{Ret} mice (Supplemental Fig. S2). Laminar targeting phenotypes were assessed in mutants and wild-type littermates (*Flrt2*^{WT}) at P15–17.

We first examined starburst arbors in *Flrt2*^{Ret} mutants. A sporadic laminar targeting phenotype was observed in mutant retina, whereby starburst neurons intermittently misprojected primarily into the S1 IPL sublayer (B,D,I). By contrast, *Flrt2*^{WT} starburst projections were confined to S2 and S4 (Fig. 2A,I; Supplemental Fig. S3A–D). A similar phenotype was observed when *Flrt2* was deleted using the starburst-specific *Chat*^{Cre} mouse, indicating that FLRT2 is functioning within starburst cells (Fig. 2I; Supplemental Fig. S3A–D). To ascertain whether starburst laminar targeting errors could involve defects in cross-circuit repulsion, we cultured primary neurons from neonatal retina and measured the overlap between starburst and GAD65$^+$ neurites. Overlap was significantly greater in *Flrt2*^{Ret} cultures compared to *Flrt2*^{WT} control cultures, suggesting a defect in cell-cell avoidance when FLRT2 is absent (Supplemental Fig. S3E,F).

We next examined ooDSGC laminar targeting in *Flrt2^{Ret}* mutants. To this end we used the *Hb9-GFP* transgene, which selectively marks ooDSGCs (Supplemental Fig. S4A,B) that prefer ventral motion[44]. Two types of ooDSGC laminar targeting alterations were observed in *Flrt2^{Ret}* animals, each of which occurred sporadically across mutant retina. First, wherever starburst arbors were mistargeted, ooDSGC dendrites remained aligned with them (Supplemental Fig. S3G), consistent with our past findings that ooDSGCs always follow starburst laminar errors[26]. Because ooDSGCs remained correctly paired with starbursts in these instances, they were scored as starburst errors rather than ooDSGC errors.

However, we also observed a second type of error – scored as ooDSGC errors – in which Hb9-DSGC dendrites became sporadically uncoupled from their starburst partners. In these cases, ooDSGC dendrites stratified within ectopic IPL regions that did not contain starburst arbors (Fig. 2E,F,H,J). These laminar errors were highly specific: When not associated with the starburst scaffold, Hb9-DSGC dendrites instead targeted stereotyped ectopic locations in S1 and S3 (Fig. 2F,H,K). Some ectopic projections extended over large distances in a minimally branched manner (Fig. 2M) – a growth pattern that differs substantially from the highly branched arbors in S2 or S4 (Fig. 2K,L). Therefore, ectopic arbors appear to represent a new dendritic growth pattern that is appended onto the normal arbor. We also observed ooDSGC laminar errors in *Six3-Cre; Flrt2$^{flox/+}$* heterozygotes, albeit at lower frequency (Supplemental Fig. S4C,D). Ectopic arbors did not co-label with the axon marker Neurofilament-M, confirming their dendritic identity (Supplemental Fig. S4E). Single-cell reconstructions revealed that ~25% of *Flrt2* mutant Hb9-DSGCs made dendritic laminar errors (Fig. 2K,L, n = 3/12 cells projected ectopically). By contrast, *Flrt2^{WT}* control animals rarely exhibited Hb9-DSGC dendrites outside the sublayers defined by starburst arbors (Fig. 2E,J). Loss of *Flrt2* also disrupted laminar targeting of a second ooDSGC subtype, marked by the *Drd4-GFP* transgene[45,46] (Supplemental Fig. S5A,B). Altogether, these *Flrt2^{Ret}* phenotypes indicate that FLRT2 influences precise laminar targeting by both starburst cells and ooDSGCs.

Cell type-specific roles for *Unc5c* and *Unc5d* in DS circuit laminar targeting

As a second way of disrupting FLRT2-UNC5C signaling, we next utilized an *Unc5c* constitutive-null allele[47,48]. Because *Unc5c$^{-/-}$* animals on a pure C57Bl6/J background rarely survived beyond P0, these experiments used a hybrid C57-SJL background (see Methods). Whereas mistargeted Hb9-DSGC arbors were rare in *Unc5c$^{+/+}$* control retinas, we found numerous ooDSGC errors in *Unc5c$^{-/-}$* mutants (Fig. 2G,J). *Unc5c$^{-/-}$* errors strongly resembled those observed in *Flrt2^{Ret}* animals, and occurred at similar frequency in each mutant, strongly suggesting that each mutation is affecting the same underlying molecular event (Fig. 2E–H,J.M; Supplemental Fig. S5C). These findings support the notion that UNC5C prevents mistargeting of ooDSGC arbors via transcellular interactions with FLRT2.

In contrast to ooDSGCs, starburst IPL projections were entirely normal in *Unc5c$^{-/-}$* mutants (Fig. 2I). We therefore considered whether a different FLRT2 binding partner might influence starburst laminar restriction. UNC5D is a close homolog of UNC5C that also binds FLRT2, and which also localizes to non-DS IPL regions in a pattern resembling UNC5C[30]. Furthermore, similar to *Unc5c*, *Unc5d* is broadly expressed by

GAD65$^+$ GABAergic amacrine cells (Supplemental Fig. S1C–E). These findings prompted us to examine DS circuit IPL targeting in *Unc5d*$^{-/-}$ mutant mice[35]. We observed a starburst IPL phenotype in *Unc5d* mutants that was strikingly similar to the *Flrt2*^{Ret} phenotype (Fig. 2C,I; Supplemental Fig. S3A–D). By contrast, Hb9-DSGC dendrite targeting was unaffected by loss of *Unc5d* (Supplemental Fig. S3H,I). Together, these results support a model in which UNC5D-FLRT2 signaling influences starburst laminar specificity, whereas UNC5C-FLRT2 signaling influences laminar specificity of ooDSGCs.

Direct FLRT2-UNC5 protein interactions mediate DS circuit laminar targeting

To critically test the model that DS circuit laminar targeting depends on direct FLRT2-UNC5C binding, we selectively disrupted FLRT2-UNC5 interactions in vivo. Structural studies have identified a FLRT ectodomain point mutation, FLRT2^{H170N} (Fig. 3A), that blocks UNC5 binding without altering trafficking, surface expression, or interactions with LPHNs[33,37]. This so-called FLRT2^{UF} mutation has been used extensively to test functional consequences of FLRT2-UNC5 signaling[32,33,37,38,49]. Using CRISPR editing, we introduced the *Flrt2*^{UF} point mutation into the mouse germline. *Flrt2*$^{UF/UF}$ animals (abbreviated *Flrt2*^{UF}) on a pure C57Bl6 background showed reduced survival beyond P0. However, similar to *Unc5c*$^{-/-}$ mice, *Flrt2*^{UF} mutants did survive and appeared grossly normal when bred on a mixed C57Bl6-SJL background. Therefore, we used this mixed background to investigate retinal phenotypes at P15–17 in *Flrt2*^{UF} mice.

Flrt2^{UF} mutants exhibited starburst (Fig. 3B–D) and ooDSGC (Fig. 3E–G) dendrite phenotypes that were strikingly similar to those observed in *Flrt2*^{Ret}, *Unc5c*$^{-/-}$, and/or *Unc5d*$^{-/-}$ mutants. Comparing *Flrt2*^{UF} to *Flrt2*^{Ret}, which completely lacks retinal *Flrt2* function, the number of starburst errors was similar (Fig. 3D). Thus, loss of UNC5 binding appears to fully account for the *Flrt2* starburst phenotype. The number of ooDSGC errors was also comparable between *Flrt2*^{UF} and *Flrt2*^{Ret} – we did not detect a statistically significant difference between the groups. However, we did note a trend towards fewer errors in *Flrt2*^{UF}, suggesting that other FLRT2 ligands may cooperate with UNC5s to mediate ooDSGC laminar targeting (Fig. 3G). Nevertheless, these findings support the conclusion that UNC5s are the major FLRT2 ligands mediating suppression of mistargeted DS circuit arbors.

Mistargeted ooDSGC arbors receive non-starburst inhibitory synapses

We next investigated whether removal of FLRT2-UNC5C signaling impacts DS circuit synaptic specificity. Normally, starburst amacrine cells provide virtually all inhibitory synapses onto ooDSGC dendrites[19,23,24,50]. However, in *Flrt2*^{Ret} and *Unc5c*$^{-/-}$ mutants, ooDSGCs send dendrites into IPL regions lacking starburst arbors (Fig. 2), suggesting that they might receive inhibitory synapses from inappropriate non-starburst partners. To test for inhibitory synapses on mistargeted Hb9-DSGC dendrites, we labeled synapses using antibodies to the presynaptic active zone marker bassoon and the inhibitory post-synaptic marker gephyrin (Fig. 4A,B; Supplemental Fig. S5D,E). We then used Object Finder software[51] to perform unbiased semi-automated identification of paired bassoon-gephyrin synapses on Hb9-GFP$^+$ arbors. We assessed both mutants but were particularly focused on *Unc5c*$^{-/-}$ animals because they lack mistargeted starburst arbors (Fig. 2I). Thus, in *Unc5c*$^{-/-}$

mutants we can be certain that starburst cells are not the source of synapses onto mistargeted ooDSGC dendrites.

This analysis revealed that mistargeted Hb9-DSGC dendrites in *Unc5c* mutants were studded with putative inhibitory synapses, at a density resembling properly localized arbors within S2 and S4 (Fig. 4C). Indeed, inhibitory synapses were identified on all mistargeted S1 and S3 arbors analyzed (n = 4 *Unc5c*$^{-/-}$, n = 4 *Flrt2*^{Ret}; 2 sections per animal). These results indicate that mistargeted Hb9-DSGC dendrites receive numerous inappropriate connections from non-DS circuit inhibitory synaptic partners – probably in both mutants, but certainly in *Unc5c*$^{-/-}$.

Maintenance of DS circuit laminar targeting mediated by FLRT2-UNC5 repulsion

To understand the mechanism by which FLRT2-UNC5 signaling controls dendritic laminar targeting, we first sought to determine the developmental events that depend on presence of these molecules. Initial formation of the DS circuit IPL sublayers is a two-step process involving stratification of starburst arbors by P2, and ooDSGC dendrites by P6[26,28] (Fig. 5A,B). Both of these events occurred normally in *Flrt2*^{Ret} and *Unc5c*$^{-/-}$ mutants, indicating that these genes are dispensable for initial circuit assembly (Fig. 5E,F; Supplemental Fig. S6).

We next investigated DS circuit laminar development between P6 and P15. This period encompasses the functional maturation of the DS circuit[52–54], and is characterized by horizontal expansion of starburst and ooDSGC arbors within S2 and S4[55–57]. In wild-type retina, we noticed a previously unreported refinement of ooDSGC lamination between P6-P15. While gross stratification of DS circuit arbors was complete by P6, we observed occasional mistargeted ooDSGC dendrites at P6 and P10 that were not paired with the starburst scaffold (Fig. 5B,C). These mistargeted dendrites were eliminated by P15 (Fig. 5D,E). In *Flrt2*^{Ret} and *Unc5c*$^{-/-}$ mutants, the number of mistargeted ooDSGC dendrites was similar to controls at P6 and P10 (Fig. 5E; Supplemental Fig S6). Subsequently however, rather than eliminating mistargeted dendrites, both mutants showed a substantial increase in mistargeting from P10-P15 (Fig. 5E). A similar phenomenon occurred for starburst arbors between P6 and P10 (Fig. 5F). These findings indicate that, even after targeting the correct IPL sublayer by P6, growing DS circuit dendrites are not exclusively confined to the appropriate sublayer. Rather, they continue to produce mistargeted branches which are eliminated in a FLRT2-UNC5-dependent manner.

UNC5s influence dendrite targeting by interfering with FLRT-LPHN adhesion

We next addressed the molecular mechanisms by which FLRT2-UNC5 binding suppresses growth of mistargeted DS circuit dendrites. One straightforward possibility is that binding initiates a repulsive signal, transduced either by FLRT2 or a co-receptor[58], that inhibits arbor growth. If this "repellent receptor" model (Fig. 6A) is correct, FLRT2 should be required cell autonomously for repulsion. To test this model we deleted *Flrt2* selectively from RGCs, using the Vglut2$^{\mathrm{Cre}}$ driver. In these *Flrt2*^{RGC} mutants, ooDSGCs laminar targeting was normal, indicating that FLRT2 is not required cell autonomously (Fig. 6B,C). Thus, FLRT2 is unlikely to function within a repellent receptor complex.

An alternate model is that FLRT2-UNC5 binding prevents elaboration of mistargeted dendrites by depriving them of FLRT2-mediated positive growth signals. FLRT adhesion can generate positive cues for synapse formation via LPHN binding[34,39]. If FLRT2-LPHN adhesion occurs among starburst and ooDSGC dendrites, this could stabilize correctly targeted nascent dendrite branches within S2 and S4 (Fig. 6D). Mistargeted branches, by contrast, would be subject to FLRT2-UNC5 binding, which is thought to diminish FLRT-LPHN adhesion through formation of the UNC5-FLRT-LPHN ternary complex[32]. As such, mistargeted dendrites encountering UNC5s may fail to receive FLRT2-LPHN positive signals, leading to their removal (Fig. 6D).

For this “adhesion-occlusion” model (Fig. 6D) to be correct, three key conditions must be met: 1) LPHNs should be expressed within developing retina and should form a ternary FLRT2-UNC5C-LPHN complex; 2) LPHNs should promote adhesion and stabilization of DS circuit dendrites; and 3) FLRT2-UNC5 binding should inhibit LPHN-mediated dendritic adhesion/stabilization. We tested each of these predictions in the following series of experiments. First, pull-down studies showed that a protein complex containing LPHN3, FLRT2, and UNC5C is indeed present in developing retina (Fig. 6E). To learn which cells express LPHNs we leveraged multiple transcriptomic datasets[42,59–61] which were in agreement that *Lphn1* and *Lphn3* are broadly expressed by most RGCs and amacrine cells, including starburst neurons and ooDSGCs. This expression pattern suggests that LPHNs are available throughout the IPL for FLRT2 binding, in which case UNC5-mediated suppression of LPHN-FLRT2 adhesion may be critical for restricting DS circuit dendrites to their appropriate sublayers (see model, Fig. 6D).

Second, to test whether LPHNs are affirmative cues for nascent DS circuit dendrites, we used an adhesion assay in which primary retinal neurons are cultured with HEK 293 cells expressing cDNAs of interest[62]. VAChT immunostaining revealed that starburst arbors associated extensively with HEK cells expressing LPHN3-GFP, but not GFP alone (Fig. 6F,G). Therefore, FLRT2$^+$ starburst cells are subject to LPHN3-mediated adhesion, which is sufficient to stabilize arbors that have contacted LPHN3$^+$ cells.

Third, to test whether UNC5s can interfere with starburst-LPHN3 adhesion, we performed the co-culture adhesion assay using HEK cells expressing both UNC5C and LPHN3. Remarkably, co-expression of UNC5C blocked starburst arbors from adhering to LPHN3 HEK cells (Fig. 6F,G). This inhibitory effect depends on transcellular binding of UNC5C to starburst FLRT2, because when we instead co-expressed a UNC5C^{UF} point mutant that cannot bind FLRTs[33], starburst adhesion to LPHN3 HEK cells was restored (Fig. 6F,G). We conclude that FLRT2-UNC5 binding inhibits FLRT2-LPHN3 adhesion, and that this anti-adhesive effect suffices to influence starburst dendrite targeting. These results support a model whereby FLRT2-UNC5 binding drives elimination of mistargeted DS circuit dendrites by depriving them of FLRT-LPHN adhesion (Fig. 6D).

UNC5C suppresses elaboration of DS circuit arbors to guide laminar targeting

A key prediction of the adhesion-occlusion model (Fig. 6D) is that UNC5 expression within non-DS circuit IPL strata renders these regions inhospitable to DS circuit dendrite growth. To test this prediction, we misexpressed UNC5C in the DS circuit IPL sublayers.

If our working model is correct, UNC5C mislocalization should impede correctly targeted DS circuit dendrites from receiving FLRT2-mediated affirmative cues, thereby diminishing growth within S2/S4 and favoring growth within ectopic sublayers (Fig. 7G,H). To misexpress UNC5C, we generated an adeno-associated virus (AAV) construct that expresses HA-tagged UNC5C protein in a Cre-dependent manner (AAV-CMV-flex-UNC5C-HA). This virus was introduced intravitreally at P1–2 into *Chat*^{Cre} transgenic mice (Fig. 7A), which express Cre recombinase selectively in starburst cells[26]. This AAV misexpression strategy is denoted Chat-UNC5C. Starburst-specific expression of UNC5C protein was validated by anti-HA immunolabeling (Supplemental Fig. S7B–E). Cre-dependent flex-tdTomato AAV was used as an injection control (Fig. 7A).

Compared to starburst cells expressing tdTomato alone, starbursts from retinal regions transduced with UNC5C AAV exhibited altered morphology consistent with impaired elaboration of arbors within sublayer S2 (Fig. 7B,C; Supplemental Fig. S7A; n = 5/5 wholemount retinas from 5 Chat-UNC5C mice). Furthermore, we observed starburst laminar targeting errors in Chat-UNC5C animals that were absent from tdTomato-only controls (Fig. 7F; n = 4/4 controls without laminar errors; n = 5/5 Chat-UNC5C with errors). These errors closely resembled the starburst phenotype in *Flrt2*^{Ret} and *Unc5d*$^{-/-}$ mutants (Fig. 2). We also observed mistargeting of Hb9-DSGC dendrites in Chat-UNC5C mice (n = 4/4 mice had errors; n = 0/4 Tomato-only controls had errors), indicating that starburst-derived UNC5C acts in a trans-cellular manner to produce ooDSGC laminar targeting errors (Fig. 7D,E). Altogether, these results indicate that ectopic UNC5C favors elaboration of mistargeted DS circuit dendrites at the expense of correctly targeted ones, as expected if UNC5s are inhibitors of FLRT2-mediated adhesion (Fig. 7G,H).

DISCUSSION

It has been suggested that affirmative cues may suffice to specify most synaptic partner choices: Inappropriate partners may be rejected simply because they lack the correct adhesive code[3,63]. However, in this study we demonstrate that negative cues also contribute in critical ways to laminar and synaptic specificity. We show that direct binding of FLRT2 to its ligands UNC5C and UNC5D serves as an error-correction mechanism for retinal DS circuit dendrites during a period of exuberant arbor growth and refinement. When FLRT2-UNC5 transcellular signals are disrupted, ooDSGCs generate ectopic dendrites that are uncoupled from their starburst partners, instead acquiring numerous inhibitory synapses from other amacrine cells. Therefore, FLRT2-UNC5 negative signals are part of the mechanism by which ooDSGCs shun inappropriate synaptic partners. This retinal function of FLRT2-UNC5 signaling is reminiscent of how the Semaphorin-Plexin system controls synaptic specificity in Drosophila ellipsoid body and mammalian spinal cord[4,64]. In all three cases, negative cues sculpt a layered neuropil, restricting circuit-specific arbors to laminae where synaptic partners are located. Thus, our study reveals common situations requiring negative synapse specificity cues, even when these cues are encoded by highly divergent molecular families.

Our findings also highlight how negative synapse specificity cues operate in concert with positive cues. We provide evidence that FLRT2-LPHN binding is part of the adhesive system that affirms DS circuit contacts, and that UNC5s exert their inhibitory effects by interfering with this adhesion. Thus, the FLRT-LPHN-UNC5 protein complex[32,37] may be a key molecular hub for synaptic choices, mediating positive wiring signals when UNC5s are absent from the complex but negative signals when UNC5s are present (Fig. 7G). Due to their widespread expression, this FLRT-LPHN-UNC5 hub may influence synaptic partner choices not only in the retina but also elsewhere in the nervous system.

Implications for understanding FLRT-UNC5 signaling mechanisms

FLRT and UNC5 proteins are emerging as important contributors to many facets of brain development and disease[31,65–69]. Previous studies have emphasized FLRTs as ligands and UNC5s as repulsive guidance receptors[35,49]. By contrast, our results reveal that signaling in the reverse direction is also possible: We show that FLRT2-expressing dendrites can be sculpted by UNC5 binding. These findings raise the intriguing possibility that FLRT2-UNC5 binding may mediate bidirectional repulsion – a mechanism that would have obvious utility in establishing discrete IPL sublayers (Fig. 1B). It will be informative to learn, in future studies, whether UNC5C- or UNC5D-expressing populations also exhibit targeting errors in *Flrt2* mutants.

Many previous studies have shown that FLRTs bind LPHNs to promote transcellular adhesion, synaptogenesis, and cell migration[34,39,40,70]. While it was known that UNC5s can form a ternary complex with LPHNs and FLRTs, the function of the complex in vivo remained unexplored. Our results suggest that inclusion of UNC5s within this complex inhibits FLRT-LPHN adhesion. While further work will be needed to prove this molecular model, our study establishes that UNC5s can counter FLRT-LPHN adhesion to control dendrite development and synaptic specificity in vivo.

Role of FLRT2-UNC5 signaling in direction-selective circuit assembly

Establishment of DS circuit IPL sublayers between P0 and P6 is driven by positive cues that pair starburst dendrites with their synaptic partners[27–29]. While prior studies presumed that starburst-ooDSGC laminar targeting was complete by P6[28,57], we show that these neurons continue to generate transient mistargeted branches during the P6-P15 period, which are eliminated in a FLRT2-UNC5 dependent manner. Why might DS circuit dendrites stray from their laminar scaffold during this time? We favor the possibility that stray arbors are an inevitable consequence of dendrite growth. The exuberant branching period coincides with a time when starbursts and ooDSGCs grow substantially in the tangential plane of the retina: adult arbor sizes are reached by ~P14[56,57,71]. Dendrites typically grow by an iterative process in which the stable portion of an arbor sprouts numerous transient processes[72,73]. Only a small subset of these sprouts survive to become part of the mature arbor[74–77]. Given this growth mechanism, it is plausible that DS circuit dendrites cannot expand in the tangential plane without inadvertently sprouting out of their sublayers. In this case, the FLRT2-UNC5-LPHN system could serve to distinguish correctly targeted dendritic sprouts from mistargeted ones.

Under this model (Fig. 7G), correctly targeted DS circuit dendritic sprouts experience stronger FLRT2-LPHN adhesion than mistargeted sprouts contacting adjacent layers, where

UNC5s interfere with FLRT-LPHN adhesion. Adhesion is a powerful pro-survival cue for nascent dendrite branches, not least because it promotes synaptogenesis[74,78] Thus, branches that experience more FLRT2-LPHN adhesion should be more likely to survive, to acquire synapses[34,39], and to become part of the mature dendrite tree. This model is strongly supported by our in vivo experiments. In wild-type retina, the adhesion differential between correct and mistargeted branches may be so great that the chance of mistargeted sprouts surviving is close to zero. However, the genetic manipulations we performed here are expected to alter this adhesion differential – either by increasing adhesion of mistargeted arbors, as when UNC5s are removed or when FLRT2 is unable to bind UNC5s; or by diminishing adhesion of correctly targeted arbors, as when starburst cells lose FLRT2 or ectopically express UNC5C. In all of these cases, mistargeted branches should experience greater relative FLRT2-LPHN adhesion, leading to stochastic stabilization of a subset of these branches which ultimately mature to become ectopic DS circuit IPL arbors. Thus, each of our genetic experiments is consistent with the working model (Fig. 7G,H).

Limitations of the study

Here we focused on FLRT2, UNC5C, and UNC5D, but other molecules also have important roles in DS circuit formation. This is evident from the fact that manipulation of FLRT2-UNC5 signaling did not prevent circuit assembly, and persistent laminar errors were seen in only a subset of ooDSGCs and OFF starburst cells. ON starbursts, meanwhile, stratified independently of FLRT2 and UNC5s. Because FLRT2-UNC5 signaling impacts pruning and refinement, rather than initial pairing of synaptic partners, it would have been surprising to find that disrupting this system completely breaks the DS circuit. Instead, pruning failures are expected to append ectopic dendrites onto the normal arbor, as we indeed observed (Fig. 2K–M). Nevertheless, the relatively limited nature of these phenotypes suggests that future work is needed to identify other molecular families that also contribute to DS circuit refinement.

Even within the gene families studied here, multiple FLRTs, UNC5s, and LPHNs are present in developing retina and poised to compensate for the loss of a single gene[79–81]. There is precedent for redundancy in DS circuit assembly: To completely disrupt adhesion between starburst and ooDSGC dendrites during the P0-P6 period, it was necessary to simultaneously knock out three cadherin genes[27]. Therefore, a more thorough disruption of the FLRT-UNC5-LPHN system might produce more profound phenotypes. We attempted to generate *Unc5c; Unc5d* double mutants but unfortunately these animals died at birth. Further work will therefore be needed to understand the full phenotypic consequences of disrupting FLRT-UNC5-LPHN signals.

STAR METHODS

RESOURCE AVAILABILITY

Lead contact—Requests for resources and reagents should be directed to and will be fulfilled by the lead contact, Jeremy Kay (jeremy.kay@duke.edu)

Materials availability—The pAAV-CMV-flex-Unc5cHA-WPRE-SV40pA plasmid has been deposited at Addgene (ID #205442). Other plasmids used in this study may be obtained as noted in the Key Resources table or from the lead contact.

The *Flrt2*^{UF} mouse line generated in this study has been deposited with the Jackson Laboratories repository (stock number 038570).

Data and code availability

- Existing, publicly available sequencing data were obtained from GEO or the Broad Institute Single Cell Portal (see Key Resources table). All microscopy and Western blot images are available upon request.
- ObjectFinder software is deposited at Zenodo. Puncta Analyzer software[82] (gift of C. Eroglu, Duke University) is available from the Eroglu lab. Please note that Puncta Analyzer has been deprecated and its key features are now incorporated into the newer SynBot software[83]. See Key Resources table for DOIs.
- Any additional information required to reanalyze the data reported in this paper is available from the lead contact upon request

EXPERIMENTAL MODEL AND STUDY PARTICIPANT DETAILS

Mice—Mouse experiments were performed according to protocols approved by the Institutional Animal Care and Use Committees at Duke University and University of California, Berkeley. Mice of both sexes were used for experiments, and we did not include or exclude animals on the basis of sex. CD1 mice were obtained from Charles River laboratory. *Flrt2*^{flox} mice (*Flrt2*$^{tm1c(EUCOMM)Wtsi}$*/RobH*) were obtained from the EMMA repository (EM: 08315). Mice carrying the *Unc5c*$^{rcmTg(Ucp)1.23Kz}$ null allele[48] were a gift of Dr. Susan Ackerman (UCSD). *Unc5d*^{tm1Kln} null mice[35] were a gift of Dr. Victor Tarabykin (Charité, Berlin) via Dr. David Feldheim (UCSC). Drd4-GFP (*Tg(Drd4-EGFP)W18Gsat*)) mice were a gift of Dr. Joshua Sanes. *Flrt2*^{UF} mice were generated in this study as described in detail below. The following strains were obtained from Jackson Labs – see Key Resources table for catalog numbers: Hb9-GFP (*B6.Cg-Tg(Hlxb9-GFP)1Tmj/J*); Six3-Cre (*Tg(Six3-cre)69Frty*)); *Chat*^{Cre} (*Chat*$^{tm2(cre)Lowl}$*/J*); Vglut2Cre (*Slc17a6*$^{tm2(cre)Lowl}$/J).

Mutant and transgenic strains were maintained on the C57Bl6/J background, and in most cases experimental animals were also on this background. For *Unc5c* null mice, experimental animals were generated on a mixed C57-SJL background as follows: First, to generate breeders, heterozygous mutants (*Unc5c*$^{+/-}$) on the C57Bl6/J background were outcrossed to SJL/J. *Unc5c*$^{+/-}$ progeny from this cross were then bred to *Unc5c*$^{+/-}$ or Hb9-GFP; *Unc5c*$^{+/-}$ animals on the pure C57Bl6 background, thereby generating mutants and wild-type littermate controls for experiments. A similar breeding strategy was used for the *Flrt2*^{UF} strain.

To generate *Flrt2*^{Ret} mutants, *Six3-Cre; Flrt2*$^{flox/+}$ mice were bred to *Flrt2*$^{flox/+}$ or *Flrt2*$^{flox/flox}$ animals with or without the Hb9-GFP transgenes. These crosses yielded *Flrt2*^{Ret} mutant animals of genotype *Six3-Cre; Flrt2*$^{flox/flox}$, as well as two types of wild-type controls 1) *Six3-Cre; Flrt2*$^{+/+}$ and 2) *flox/+* or *flox/flox* animals without the Cre transgene.

These were phenotypically indistinguishable and so were pooled as *Flrt2*^{WT} animals. A similar breeding strategy was used with Vglut2$^{\text{Cre}}$ mice to generate *Flrt2*^{RGC} mutants.

For all strains, P1-P6 neonates were euthanized by ice anesthesia followed by decapitation. Mice aged P7 and older were euthanized via isoflurane anesthesia followed by decapitation.

Primary cultures and cell lines—Primary cultures of retinal neurons were prepared using P0/P1 mice obtained from CD1 timed pregnant litters (Charles River). Cultures were grown at 37° C in neuronal growth medium[84] containing MEM + B27 supplement and 5% fetal bovine serum.

HEK 293T cells were obtained from ATCC and grown at 37°C in DMEM containing 10% fetal bovine serum. For co-cultures with primary neurons, neuronal growth medium was used.

METHOD DETAILS

Generation of *Flrt2*^{UF} mice—To engineer the *Flrt2*^{UF} mutation (H170N)[33] into the mouse genome, we used a CRISPR-Cas9 homology-directed repair strategy. We generated a 200 bp repair oligonucleotide homologous to the region surrounding the codon encoding amino acid H170. In this oligonucleotide the CAC H170 codon was mutated to AAC (N). To induce homology-directed repair at the appropriate genomic site, a single guide RNA (sgRNA) was produced in which the PAM sequence overlaps the H170 codon (sequence 5’ GCCCAACAGGCACGCTACTCagg; PAM site is denoted by lowercase letters). The PAM sequence is destroyed by the codon-altering mutation, thereby rendering correctly edited alleles immune to further Cas9 cutting activity. See Key Resources table for sequences.

The repair DNA was electroporated into one-cell stage B6SJLF1/J embryos together with pre-assembled Cas9-sgRNA ribonucleoproteins, as described[85]. Briefly, to generate sgRNA for electroporation, a DNA template was generated by PCR and then used for RNA synthesis (HiScribe T7 RNA polymerase, NEB #E2040S). DNA template was removed from the reaction with Turbo DNAse (Invitrogen #AM2238). The sgRNA was purified by phenol/chloroform extraction, ethanol precipitated, and resuspended in nuclease-free H_2O. The Cas9 ribonucleoprotein was assembled by incubating Cas9 protein, sgRNA, and repair oligo together for 10 min at 37°C in Tris (2-carboxyethyl) phosphine hydrochloride (TCEP) buffer[85]. The ribonucleoprotein mix was electroporated using a NEPAGENE Super Electroporator (NEPA21 Type II) using a glass slide chamber with platinum electrodes (Bulldog Bio part CUY501P1–1.5) with the following settings: Poring Pulse: V 40, Length(ms) 3.5, Interval (ms)50, No 4, D. Rate % 10, Polarity +; Transfer Pulse: V 7, length (ms) 50, Interval (ms) 50, No. 5, D. Rate% 40, Polarity +/−. Following electroporation the embryos were transferred to pseudopregnant females.

To screen founders for the correctly modified allele, founder genomic DNA was prepared from tail and/or toe tissue and subject to PCR using primers targeting the ends of the repair oligonucleotide homology region (Sense: ‘ 5’ accgcggtggcggcc GCT CCT CAA GCT GGA AGA ACT CCA 3’; Antisense: 5’ tagaggatccactag TGT CTG ATA TGA CGG CAA TTC GGT 3’). PCR products were subject to Sanger sequencing using Sense primer. For animals in which sequencing revealed InDels across the target region, the PCR fragments containing InDels were cloned into pL253 at the NotI and SpeI sites via InFusion cloning (Takara #ST0344). Bacterial recombinants were screened via PCR using primers 253.S (caaggcgattaagttgggtaac) and 253.AS (gcgtgttcgaattcgccaatgac). Plasmid DNA from positive clones were sequenced using Sense primer for verification of the targeted mutation. Positive founders were backcrossed to C57Bl6/J. Subsequently, the line was maintained in the same manner.

To genotype the UF dinucleotide point mutation by PCR, we used a 4 primer strategy[86] in which “outer” primers in constant regions combine with “inner” primers overlapping the point mutation site to distinguish the wild-type and mutant alleles. Primer sequences are given in the Key Resources table. Band sizes: Outer, 599 bp. Inner mutant, 426 bp. Inner wild-type, 231 bp.

Cell culture—Primary cultures of P0/P1 retinal neurons were prepared from CD1 timed pregnant litters (Charles River). The procedure was modified from the protocol of Jiang et al. (2019). Retinas were isolated from the eyecup in dissecting solution[84], followed by incubation in 0.5% Trypsin for 15–20 min at 37°C with gentle intermittent mixing. Next, trypsin was exchanged two times with dissecting solution and reaction was stopped using stopping solution (HBSS + 5% serum). Trypsinized retina was triturated 4 times either in stopping solution or MEM1X solution and centrifuged for 5 mins at 800 × g at 4°C. Cells were resuspended in 1.0 ml of plating medium[84] and filtered through 30 μm sterile filter. Isolated cells were plated at density of ≥ 200,000 cells/well on previously coated Poly L-lysine coverslips. Cells were allowed to settle for 30 mins in cell culture incubator, at which time 2 ml of plating medium was added into each well. Cells were incubated for 1 day at 37°C. On the next day, media was exchanged for neuronal growth medium[84] containing B27 supplement. On day 4, AraC (cytosine arabinoside) was included in the neuronal growth medium. Cultures were fixed on day 10–12.

For GAD65-VAChT, overlap analysis, confocal stacks were acquired from GAD65 + VAChT immunostained cultures and single z slices chosen for analysis. Overlap analysis[87] was performed with coloc2 ImageJ plugin. The overlap ratio was calculated as the VAChT pixel intensities within pixels containing non-zero GAD65 values, divided by total VAChT pixel intensity across the image. This yields a measure of overlap between the two signals that is independent of overall image brightness[87].

For the co-culture cell adhesion assay, primary cultures were prepared as described above, and transfected HEK 293 cells were added to the culture on day 8. The day prior to co-culture, HEK cells were transfected with the following plasmids: CMV-EGFP; CMV-Lphn3-GFP encoding full-length LPHN3[34]; CMV-Unc5c-Flag encoding full-length UNC5C[30]; or CMV-Unc5c^{UF}-Flag encoding the mutant UNC5C protein that is impaired in binding FLRTs[33]. Transfected cells were co-cultured with primary cells for 2 days, then fixed in 2% paraformaldehyde/1x PBS and subjected to immunohistochemistry. Data are from three independent replicates of the experiment; these did not show significant batch effects so they were pooled for presentation in Fig. 6G.

In Situ Hybridization—Eyes from euthanized P6 wildtype mice (CD-1 or B6;SJL strains) were fixed in 4% paraformaldehyde in PBS for 24 hours at RT and then washed 3X with PBS. In situ hybridization was performed with two independent RNA labeling technologies – RNAScope (Advanced Cell Diagnostics, Newark, CA) and hybridization chain reaction (HCR; Molecular Instruments, Los Angeles, CA).

For RNAScope, isolated retinas were cryoprotected in 30% sucrose and 0.02% sodium azide in PBS and frozen in Tissue Freezing Medium (General Data; Cincinnati, OH). Retinas were cryosectioned at 16 μm and mounted on Superfrost Plus slides. Retinal sections were pre-treated according to manufacturer’s instructions for fixed frozen tissue. Probes to *Unc5c* and *Gad2* (i.e. Gad65) were from the standard ACD catalog. Probes were hybridized and amplified according to manufacturer’s instructions using the RNAscope Fluorescent Multiplex Kit.

For HCR labeling, fixed eyes were methanol-habituated as follows: 5 minute washes, rocking, on ice, first in 25% methanol, then 50% methanol, 75% methanol, and two 100% methanol washes. Eyecups were cryoprotected as above and cryosectioned at 20 μm. Sections were stained with in situ Hybridization Chain Reaction (HCR) probes for *Gad2* and *Unc5c*, from Molecular Instruments following Molecular Instruments’ protocol for HCR RNA-FISH in fixed frozen tissue sections. The only deviations from this protocol are as follows: slides were treated with Proteinase K for 5 minutes; 0.8 μL of each probe was added to 150 μL probe hybridization buffer for each slide; slides were stained with Hoechst for 30 min at room temperature before amplification hairpins were washed off.

Following staining with either method, sections were imaged on a Nikon A1 confocal system. Z-stacks of 0.33 μm steps were acquired using a 60X objective (Plan Apochromat, NA 1.40) with oil immersion. Stacks were imported into FIJI[88]; single optical slices (or a Z-projection of a subset of the stack) are shown here for illustration purposes but the full Z-stack was used for quantification. To quantify RNA signals, the multi-point tool in FIJI was used to manually mark each nucleus that was positive for the probe. Positive cells were called based on the presence of punctate RNA signal overlapping the nuclear counterstain signal (Fig. 1G). *Unc5c* and *Gad2* channels were analyzed individually to blind the co-expression analysis. Co-expression of markers was used to calculate fraction of *Unc5c* mRNA$^+$ cells that expressed *Gad2* mRNA. Two sections were quantified for each animal.

Single cell RNA-seq—Single-cell RNA-seq data from FACS-purified amacrine cells[42], adult RGCs[61], or developing RGCs[80] were obtained from the Broad Institute Single Cell Portal as a normalized count matrix, along with the published cluster annotations and UMAP coordinates for each cell. These were loaded into Seurat software[89] for analysis and to generate the gene expression data shown in Supplemental Fig. S1. Data from a separate P5 RGC dataset[60] was accessed via a web-based interface. Cell types within that dataset were identified based on cluster correspondences determined by Shekhar et al.[80]

To assign amacrine clusters as *Unc5c*-positive or −negative (Supplemental Fig. S1E), we took into account overall expression level across all cells in the cluster (average expression >

0) as well as the fraction of expressing cells within the cluster (a minimum of 20% of cells needed to express the gene to call the cluster positive).

Immunohistochemistry—For immunohistochemistry, age-matched mouse eyes of both sexes were collected following euthanasia. Eyes were fixed in 4% paraformaldehyde in PBS for 90 min on ice, then corneas and lenses were removed. To label synapses, lenses were removed prior to fixation and eye cups were fixed in 4% paraformaldehyde in PBS for 45 mins on ice. For retinal cross sections, eye cups were cryoprotected in 30% sucrose and 0.02% sodium azide in PBS, frozen in Tissue Freezing Medium (Triangle Biomedical), cryostat sectioned at 20 μm, and placed on Superfrost Plus slides. Sections were blocked in 3% normal donkey serum in PBS with 0.3% Triton X-100 for 1h at room temperature (RT). For retinal flat mounts, retinas were dissected out of eye cups prior to histology, then blocked for 1–2h at RT. Rat anti-mouse Fc block 1:400 (553142, BD Biosciences) was included in the blocking solution for experiments involving mouse antibodies. The following primary antibodies were used: Guinea pig anti-bassoon 1:500 (141004, Synaptic Systems); goat anti-ChAT 1:400 (AB144P, Millipore); goat anti-FLRT2 1:250 (AF2877 R&D Systems); mouse anti-GAD65 1:1000 (MAB351, EMD Millipore); mouse anti-gephyrin 1:700 (147021, Synaptic Systems); rabbit anti-GFP 1:500 (AB3080P, Millipore); goat anti-GFP 1:500 (ab5450, Abcam); rat anti-Neurofilament-M 1:500 (2H3, Developmental Studies Hybridoma Bank); rabbit anti-Satb1/2 1:500 (2938–1, Epitomics); guinea pig anti-VAChT 1:500 (AB1588, Millipore); mouse anti-Flag 1:1000 (clone M2, F1804, Sigma); rat anti-HA 1:500 (11867423001, Sigma); rabbit anti-mCherry 1:1000 (EMU106, Kerafast). Antibodies were diluted in blocking solution, then applied to retinal sections and incubated overnight at 4°C. For flat mounts, 0.02% sodium azide was included in the primary antibody solution and incubation proceeded for 5–7 d at 4°C on a rocker. Sections were washed three times in PBS and fluorophore-conjugated Jackson ImmunoResearch secondary antibodies were applied at 1:1000 for 2h at RT. The following secondaries were used: Alexa Fluor 488 Donkey Anti-Rabbit [711–545-152]; Cy3 Donkey Anti-Goat [705–165-147]; Cy3 Donkey Anti-Guinea Pig [706–165-148]; Alexa Fluor 647 Donkey Anti-Goat [705–605-147]; Alexa Fluor 647 Donkey Anti-Guinea Pig [706–605-148]; Alexa Fluor 647 Donkey Anti-Mouse [715–605-151]; Alexa Fluor 647 Donkey Anti-Rat [712–605-153]. Slides were washed 3 times in PBS then mounted with Fluoromount G. For wholemounts, retinas were washed several times in PBS over 2–4h at RT on a rocker, then secondary antibodies incubated overnight at 4°C on a rocker. Wholemounts were then washed several times on a rocker at RT over 2 hours, mounted on Superfrost slides, coverslipped, and mounted with Fluoromount G.

Western blots and co-immunoprecipitation—Retinas were isolated in dissecting solution: 1X HBSS containing 10mM HEPES and 4mM NaHCO3. Isolated retinas were suspended in lysis buffer containing 100 mM Tris-HCl, pH 8.0, 150 mM NaCl, 1 mM EDTA, and 1%Triton X-100 for 45 min on vertical rotator at 4°C. The sample was vortexed briefly to break up larger pieces of tissue. The sample was sonicated at 20% output of ultrasonicator with pulse ON/OFF cycle for approximately 10 times on ice. Afterward, the lysate was centrifuged at 5,000 rpm for 5 mins at 4°C. The supernatants were transferred into new Eppendorf tubes and centrifugation step was repeated one more time to clear the lysate.

For co-immunoprecipitation (IP) experiments, retina lysates were prepared from a complete litter of P6 CD-1 mice (n = 10 animals). The cleared lysate was split in two equal volumes which were used for experimental (anti-LPHN3) or control (mouse IgG) conditions. For each sample, 5 μg of normal mouse IgG (control) or LPHN3 purified monoclonal antibody was added to the lysate and incubated with gentle mixing at 4°C for 1 hour. Next, 25 μL of Protein A/G beads (Pierce) were added to each sample and incubated overnight at 4°C. The next day, beads were allowed to settle and kept on magnetic apparatus to pull beads away and supernatant was discarded. Dynabeads were washed 3 times with 1X PBS. Lastly, beads were boiled in 10 μL of 4X denaturing sample buffer dye and 10μL of 1XPBS, subjected to SDS-PAGE, and blot transferred onto nitrocellulose membrane. The membranes were incubated with primary antibodies in LI-COR blocking solution overnight at 4°C. Primary antibodies used were: LPHN3[90] (1:500), UNC5C (1:1000) and FLRT2 (1:500). On the next day, the blot was washed 3 times with 1X PBS for 5 min at room temperature. The blot was incubated with LI-COR secondary antibody at dilution of 1:5000 for 1hr RT. The washing step was repeated and subsequently blots were imaged in LI-COR Odyssey imaging system.

For Western blotting of AAV-injected eyes, lysates were prepared at P8 (7 days post-injection) from 2 *Chat*^{Cre} pups per virus condition (i.e. 4 eyes with flex-tdTomato control and 4 eyes with flex-tdTomato + flex-Unc5c-HA). Sample preparation, blotting, and staining procedures were as described above. Primary antibody was rat anti-hemagglutinin (HA) at 1:500 dilution.

Synapse density in IPL—For quantification of synapses, images were acquired using a Nikon A1 confocal system. Z-stacks (106 μm × 106 μm × 0.33 μm step size; 9–15 steps/z-stack) were acquired using a 60X objective (Plan Apochromat, NA 1.49) with oil immersion and 2X optical zoom. Three independent fields of view (FOV) were used for analysis of ON and OFF sublaminae for each animal (n = 3). All FOV were sampled from a similar retinal eccentricity. Images were deconvolved using Nikon Elements Extended Resolution plugin, then imported into ImageJ. Minor brightness/contrast adjustments were made similarly across all images. Maximum intensity projections of three consecutive 0.33 μm z-sections (for a total z-depth of 1 μm) were used for synapse analysis using the Puncta Analyzer plugin for ImageJ[82]. 3–5 maximum intensity projections were averaged to obtain the number of colocalized puncta per field (dots on graphs). The border between OFF and ON sublaminae was defined based on histologic landmarks[91]. Puncta Analyzer was used to count synapses based on colocalization of presynaptic and postsynaptic markers as previously described[82,91]. In brief, the projected images were divided into individual channels (presynaptic and postsynaptic markers); background was subtracted for each channel (rolling ball radius = 50); thresholds were adjusted manually to detect individual puncta while minimizing background; and puncta smaller than 4 pixels were filtered out. For all conditions, $N = 3$ animals per genotype, with 3 FOV per animal. Single slices of the z-stacks were chosen for presentation of representative images. Standard error was calculated from 9 FOV from 3 animals per genotype.

Synapse identification on ooDSGC dendrites—To visualize the distribution of synaptic puncta along dendrites of GFP-labeled ooDSGCs, we utilized a semi-automated method of synapse identification[51]. Images of of synaptic puncta were acquired at a voxel size of 0.104 × 0.104 × 3 µm, deconvolved using Nikon Elements software, and then converted to 8-bit in ImageJ. Using the Simple Neurite Tracer plugin for ImageJ[92], we generated a 3D mask of the GFP channel and then used a MATLAB application Object Finder[51] to identify synaptic puncta within the mask. Object Finder was run with the following settings to segment bassoon and gephyrin puncta: Expected size range = 0.2–5.0 µm; algorithm = iterative thresholding; connectivity = 6; noise estimation = standard deviation; watershed, block search, local noise = true; minimum object intensity = 2x above noise; exclude if single z plane = true. For calling synapses, the minimum overlap between segmented bassoon and gephyrin voxels was set to 50%.

Analysis of laminar targeting phenotypes—Retinal cross sections (20 µm) were prepared from P6, P10, or P15 animals. Each section was collected sequentially on a series of microscope slides, such that each slide contained an evenly-spaced series of sections (200 µm section interval). For counting of laminar errors, 2–3 sections per animal were chosen for analysis. The chosen sections were separated by at least 100 µm – larger than most of the observed errors – so as to minimize the chances of counting the same error in multiple sections. The chosen sections were also limited to the most central portion of the tissue block, such that sections were as perpendicular as possible to the IPL layers. This selection was crucial to ensure that tissue curvature did not influence scoring of IPL sublaminar position.

Each chosen section was manually inspected for laminar targeting errors using fluorescence microscopy, and all instances of mistargeted dendrites within the section were counted. “Starburst errors” were defined as VAChT$^+$ arbors ramifying above or below the main S2 or S4 VAChT bands. “ooDSGC errors” were defined as GFP$^+$ arbors that resided in ectopic sublayers and were uncoupled from the starburst scaffold. (When ooDSGC dendrites followed starburst arbors into an ectopic sublayer, this was only counted as a starburst error). Notably, we could not distinguish the number of different cells contributing dendrites to these mistargeted laminar fascicles, so each instance was counted only as a single error. If an error was seen at the same retinal location in multiple sections, it was only counted once, to rule out the possibility that the same mistargeted dendrites might extend across the 100 µm section distance and be counted twice. Confocal z-stacks (0.3–1.0 µm z step) were taken for each region of interest containing an error. While single confocal slices (or a Z-projection of a subset of the stack) are shown here for illustration purposes, each error was verified by examining the full confocal stack. For each section analyzed, the end-to-end length of the IPL was measured in FIJI using the Freehand Line tool. This length was then used to express the number of targeting errors observed in each section as errors per millimeter.

Satb1 co-labeling[28] was used to confirm that the vast majority Hb9-GFP$^+$ cells are *bona fide* ooDSGCs at the ages used in this study (Supplemental Fig. S4A,B). When Satb1-negative GFP cells were observed, they were always located in the far peripheral retina. Therefore, for Hb9-ooDSGC analysis, the two most peripheral 60X fields of view (FOVs) were not used because these FOVs occasionally include ganglion cells that are not ooDSGCs

(Supplemental Fig. S4A,B). Phenotype graphs show averaged data from at least 2 sections per animal. Control groups in these graphs show pooled wild-type littermate data from *Flrt2* and *Unc5c* strains, as these different controls did not show phenotypic differences.

Mistargeted arbors were represented graphically by generating fluorescence profile plots through the IPL using FIJI. Raw data were exported to Excel, and for each channel the background signal was subtracted and resulting values were normalized to signal maxima. Images were median filtered (radius = 0.5 pixels) to remove background noise from photomultiplier tube.

For en-face imaging of ooDSGC laminar errors in retinal wholemounts, confocal z-stacks were acquired through the depth of the IPL at a z resolution of 0.4 – 0.6 μm. Representative images shown in Fig. 2M depict a maximum projection of a small number of z-slices (encompassing approximately 1 μm of z distance), acquired at the level of the INL/IPL border. This region does not normally contain ooDSGC dendrites in wild-type retina.

Two-photon guided morphological reconstructions—Isolated whole retinas from adult (~P40) mice were micro-cut at the dorsal and ventral halves to allow flattening, with dorsal and ventral mounted over a 1–2 mm^2 hole in nitrocellulose filter paper (Millipore) with the photoreceptor layer side down and stored in oxygenated Ames' media (maximum 10 h).

Identification, dye loading and imaging of GFP$^+$ ooDSGCs was performed as described previously[93]. In brief, GFP$^+$ cells were identified using a custom-modified two-photon microscope (Fluoview 300; Olympus America) tuned to 920 nm to minimize activation and bleaching of photoreceptors. The inner limiting membrane above the targeted cell was dissected using a glass electrode. Cell attached voltage clamp recordings were performed with a new glass electrode (4–5 MΩ) filled with internal solution containing the following (in mM): 110 CsMeSO4, 2.8 NaCl, 20 HEPES, 4 EGTA, 5 TEA-Cl, 4 Mg-ATP, 0.3 Na_3GTP, 10 Na_2Phosphocreatine, QX-Cl and Alexa-594 Hydrazide dye (pH = 7.2 with CsOH, osmolarity = 290, $ECl^- = -60$ mV). Signals were acquired using Clampex 10.4 recording software and a Multiclamp 700A amplifier (Molecular Devices), sampled at 10 kHz, and low pass filtered at 6 kHz. The Alexa dye freely diffused into the ooDSGC cytoplasm after obtaining a giga ohm (1GΩ) seal and breaking into the cell membrane. Cells were imaged for electrode positioning using two photon excitation at 800 nm. At this wavelength, GFP is not efficiently excited thereby preserving fluorescence for anatomical imaging.

Next, morphological reconstruction and dendritic segmentation were performed as described previously[93]. Briefly, 480 × 480 μm Image stacks were acquired at z intervals of 1.0 μm and resampled fifteen times for each stack using a 20X objective (Olympus LUMPlanFl/IR 2x digital zoom, 1.0 NA) and 30kHz resonance scanning mirrors covering the entire dendritic fields of the ooDSGCs. Image stacks of ooDSGCs were then imported to FIJI and a custom macro was used to segment ON and OFF dendrites based on their lamination depth in the inner plexiform layer (ON layer 10–30 μm, OFF layer 35–55 μm depth). Following ON and OFF dendritic segmentation, we used the Simple Neurite Tracer plugin on FIJI to skeletonize and then binarize the ON and OFF dendritic segments for morphological analyses.

UNC5C gain of function—For AAV production we generated a *ITR-CMV-flex-Unc5cHA-WPRE-SV40pA-ITR* construct. A cDNA encoding *Unc5c*[30] was tagged at the 3' end with a 3xHA epitope tag and cloned behind a mini-CMV promoter containing the MVM small intron. Cre-dependence of expression was conferred using the flex-switch strategy[94]. AAV particles of serotype PHP.eB were produced from this plasmid by the Duke Viral Vector Core. CAG-flex-tdTomato viral particles (gift of Edward Boyden) was purchased from Addgene (Addgene viral prep #28306-PHPeB).

For AAV administration, heterozygous $Chat^{Cre}$ P1–2 neonatal mice were anesthetized on ice until unresponsive to toe pinch. Eyelids were cleaned with an ethanol wipe, then a guide hole was punctured at the outer edge of the ora serrata using a 30G needle. A Hamilton syringe was used to inject 0.5–0.75 ul of virus and 1:10 FastGreen was included to visualize injection success. Left eyes were injected with a 5:1 mixture of experimental virus (AAV-flex-Unc5c-HA) and tdTomato reporter virus (AAV-flex-tdTomato); right eyes were injected with the tdTomato reporter virus alone as control. Mice were recovered on a heated pad until they regained pinkness and light aversion. Pups were returned to their home cage with mother after recovery. After 4 weeks, mice were sacrificed and eyes were harvested for histology. Anti-HA staining was performed on each retina to confirm UNC5C protein expression. To confirm the timing of UNC5C-HA expression, a cohort of animals was also collected 1 week post-injection and was subjected to anti-HA immunostaining and Western blotting (Supplemental Fig. S7B).

For phenotypic analysis, an evenly-spaced series of 20 μm cryosections was prepared and selected for analysis as described in “Analysis of laminar targeting phenotypes” above. To ensure accuracy of laminar scoring results, only sections through the most central portion of the retina, perpendicular to the IPL sublayers, were selected for analysis. In each analyzed section, retinal regions containing virally transduced cells were identified using tdTomato expression. Laminar errors were then scored within these regions.

QUANTIFICATION AND STATISTICAL ANALYSIS.

Statistical tests were performed using GraphPad Prism software. Non-parametric tests were used in many cases, because large numbers of “0” values (typically in the control condition) led to non-normal data distributions. Sample sizes, statistical tests used, and P-values are given in figure legends and graphs where applicable; otherwise they are given in Results.

Supplementary Material

Refer to Web version on PubMed Central for supplementary material.

ACKNOWLEDGEMENTS

Funding was provided by the National Eye Institute (EY027998 to C.L.P; EY024694 and EY031445 to J.N.K; EY005722 to Duke University; and EY007551 to University of Houston); National Institute of Neurological Disorders and Stroke (NS106756 to M.E.Q.); Research to Prevent Blindness (Unrestricted Grant to Duke

University); and a Glaucoma Research Foundation Shaffer Grant (to L.D.S.). We thank Woj Wojtowicz for reagents and helpful discussions; Ariane Pendragon and William Kornahrens for technical assistance; Gary Kucera and Cheryl Bock (Duke Transgenic Mouse Shared Resource) for generating *Flrt2*^{UF} mice; Boris Kantor (Duke Viral Vector Core) for providing AAVs; and Susan Ackerman, Joshua Sanes, Victor Tarabykin, and David Feldheim for sharing mouse lines.

DIVERSITY AND INCLUSION

One or more of the authors of this paper self-identifies as an underrepresented ethnic minority in their field of research or within their geographical location. One or more of the authors of this paper self-identifies as a gender minority in their field of research.

REFERENCES

1. Sanes JR, and Zipursky SL (2020). Synaptic Specificity, Recognition Molecules, and Assembly of Neural Circuits. Cell 181, 536–556. 10.1016/j.cell.2020.04.008. [PubMed: 32359437]
2. Prigge CL, and Kay JN (2018). Dendrite morphogenesis from birth to adulthood. Curr. Opin. Neurobiol. 53, 139–145. 10.1016/j.conb.2018.07.007. [PubMed: 30092409]
3. Lefebvre JL, Sanes JR, and Kay JN (2015). Development of dendritic form and function. Annu. Rev. Cell. Dev. Biol. 31, 741–777. 10.1146/annurev-cellbio-100913-013020. [PubMed: 26422333]
4. Pecho-Vrieseling E, Sigrist M, Yoshida Y, Jessell TM, and Arber S (2009). Specificity of sensory–motor connections encoded by Sema3e–Plxnd1 recognition. Nature 459, 842–846. 10.1038/nature08000. [PubMed: 19421194]
5. Kolodkin AL, and Tessier-Lavigne M (2011). Mechanisms and molecules of neuronal wiring: a primer. Cold Spring Harbor perspectives in biology 3, 1–14. 10.1101/cshperspect.a001727.
6. Cang J, and Feldheim DA (2013). Developmental mechanisms of topographic map formation and alignment. Annu. Rev. Neurosci. 36, 51–77. 10.1146/annurev-neuro-062012-170341. [PubMed: 23642132]
7. Pederick DT, Lui JH, Gingrich EC, Xu C, Wagner MJ, Liu Y, He Z, Quake SR, and Luo L (2021). Reciprocal repulsions instruct the precise assembly of parallel hippocampal networks. Science 372, 1068–1073. 10.1126/science.abg1774. [PubMed: 34083484]
8. Sun LO, Jiang Z, Rivlin-Etzion M, Hand R, Brady CM, Matsuoka RL, Yau K-W, Feller MB, and Kolodkin AL (2013). On and off retinal circuit assembly by divergent molecular mechanisms. Science (New York, N.Y.) 342. 10.1126/science.1241974.
9. Matsuoka RL, Nguyen-Ba-Charvet KT, Parray A, Badea TC, Chédotal A, and Kolodkin AL (2011). Transmembrane semaphorin signalling controls laminar stratification in the mammalian retina. Nature 470, 259–263. 10.1038/nature09675. [PubMed: 21270798]
10. Patterson SS, Bembry BN, Mazzaferri MA, Neitz M, Rieke F, Soetedjo R, and Neitz J (2022). Conserved circuits for direction selectivity in the primate retina. Curr. Biol. 32, 2529–2538 e2524. 10.1016/j.cub.2022.04.056. [PubMed: 35588744]
11. Kim YJ, Peterson BB, Crook JD, Joo HR, Wu J, Puller C, Robinson FR, Gamlin PD, Yau KW, Viana F, et al. (2022). Origins of direction selectivity in the primate retina. Nat Commun 13, 2862. 10.1038/s41467-022-30405-5. [PubMed: 35606344]
12. Mauss AS, Vlasits A, Borst A, and Feller M (2017). Visual Circuits for Direction Selectivity. Annu. Rev. Neurosci. 40, 211–230. 10.1146/annurev-neuro-072116-031335. [PubMed: 28418757]
13. Giolli RA, Blanks RH, and Lui F (2006). The accessory optic system: basic organization with an update on connectivity, neurochemistry, and function. Prog. Brain Res. 151, 407–440. 10.1016/S0079-6123(05)51013-6. [PubMed: 16221596]
14. Fredericks CA, Giolli RA, Blanks RH, and Sadun AA (1988). The human accessory optic system. Brain Res. 454, 116–122. 10.1016/0006-8993(88)90809-8. [PubMed: 3408998]
15. Hamilton NR, Scasny AJ, and Kolodkin AL (2021). Development of the vertebrate retinal direction-selective circuit. Dev. Biol. 477, 273–283. 10.1016/j.ydbio.2021.06.004. [PubMed: 34118273]

16. Ray TA, and Kay JN (2015). Following Directions from the Retina to the Brain. Neuron 86, 855–857. 10.1016/j.neuron.2015.05.017. [PubMed: 25996129]

17. Briggman KL, Helmstaedter M, and Denk W (2011). Wiring specificity in the direction-selectivity circuit of the retina. Nature 471, 183–188. 10.1038/nature09818. [PubMed: 21390125]

18. Fried SI, Münch T.a., and Werblin FS (2002). Mechanisms and circuitry underlying directional selectivity in the retina. Nature 420, 411–414. 10.1038/nature01179. [PubMed: 12459782]

19. Yoshida K, Watanabe D, Ishikane H, Tachibana M, Pastan I, and Nakanishi S (2001). A key role of starburst amacrine cells in originating retinal directional selectivity and optokinetic eye movement. Neuron 30, 771–780. [PubMed: 11430810]

20. Hanson L, Sethuramanujam S, deRosenroll G, Jain V, and Awatramani GB (2019). Retinal direction selectivity in the absence of asymmetric starburst amacrine cell responses. Elife 8. 10.7554/eLife.42392.

21. Vaney DI, and Pow DV (2000). The dendritic architecture of the cholinergic plexus in the rabbit retina: selective labeling by glycine accumulation in the presence of sarcosine. J. Comp. Neurol. 421, 1–13. [PubMed: 10813769]

22. Pei Z, Chen Q, Koren D, Giammarinaro B, Acaron Ledesma H, and Wei W (2015). Conditional Knock-Out of Vesicular GABA Transporter Gene from Starburst Amacrine Cells Reveals the Contributions of Multiple Synaptic Mechanisms Underlying Direction Selectivity in the Retina. J Neurosci 35, 13219–13232. 10.1523/JNEUROSCI.0933-15.2015. [PubMed: 26400950]

23. Bleckert A, Zhang C, Turner MH, Koren D, Berson DM, Park SJH, Demb JB, Rieke F, Wei W, and Wong RO (2018). GABA release selectively regulates synapse development at distinct inputs on direction-selective retinal ganglion cells. Proc Natl Acad Sci U S A 115, E12083–E12090. 10.1073/pnas.1803490115. [PubMed: 30509993]

24. Sivyer B, Tomlinson A, and Taylor WR (2019). Simulated Saccadic Stimuli Suppress ON-Type Direction-Selective Retinal Ganglion Cells via Glycinergic Inhibition. J Neurosci 39, 4312–4322. 10.1523/JNEUROSCI.3066-18.2019. [PubMed: 30926751]

25. Stacy RC, and Wong ROL (2003). Developmental relationship between cholinergic amacrine cell processes and ganglion cell dendrites of the mouse retina. J. Comp. Neurol. 456, 154–166. 10.1002/cne.10509. [PubMed: 12509872]

26. Ray TA, Roy S, Kozlowski C, Wang J, Cafaro J, Hulbert SW, Wright CVE, Field GD, and Kay JN (2018). Formation of retinal direction-selective circuitry initiated by starburst amacrine cell homotypic contact. eLife 7, e34241. 10.7554/eLife.34241. [PubMed: 29611808]

27. Duan X, Krishnaswamy A, Laboulaye MA, Liu J, Peng Y-R, Yamagata M, Toma K, and Sanes JR (2018). Cadherin Combinations Recruit Dendrites of Distinct Retinal Neurons to a Shared Interneuronal Scaffold. Neuron 99, 1145–1154.e1146. 10.1016/j.neuron.2018.08.019. [PubMed: 30197236]

28. Peng YR, Tran NM, Krishnaswamy A, Kostadinov D, Martersteck EM, and Sanes JR (2017). Satb1 Regulates Contactin 5 to Pattern Dendrites of a Mammalian Retinal Ganglion Cell. Neuron 95, 869–883.e866. 10.1016/j.neuron.2017.07.019. [PubMed: 28781169]

29. Duan X, Krishnaswamy A, De la Huerta I, and Sanes JR (2014). Type II cadherins guide assembly of a direction-selective retinal circuit. Cell 158, 793–807. 10.1016/j.cell.2014.06.047. [PubMed: 25126785]

30. Visser JJ, Cheng Y, Perry SC, Chastain AB, Parsa B, Masri SS, Ray TA, Kay JN, and Wojtowicz WM (2015). An extracellular biochemical screen reveals that FLRTs and Unc5s mediate neuronal subtype recognition in the retina. eLife 4, e08149. 10.7554/eLife.08149. [PubMed: 26633812]

31. Klein R, and Pasterkamp RJ (2021). Recent advances in inter-cellular interactions during neural circuit assembly. Curr. Opin. Neurobiol. 69, 25–32. 10.1016/j.conb.2020.12.004. [PubMed: 33383489]

32. Jackson VA, Mehmood S, Chavent M, Roversi P, Carrasquero M, del Toro D, Seyit-Bremer G, Ranaivoson FM, Comoletti D, Sansom MSP, et al. (2016). Super-complexes of adhesion GPCRs and neural guidance receptors. Nature Communications 7, 11184. 10.1038/ncomms11184.

33. Seiradake E, del Toro D, Nagel D, Cop F, Härtl R, Ruff T, Seyit-Bremer G, Harlos K, Border EC, Acker-Palmer A, et al. (2014). FLRT structure: balancing repulsion and cell adhesion in

cortical and vascular development. Neuron 84, 370–385. 10.1016/j.neuron.2014.10.008. [PubMed: 25374360]

34. O'Sullivan ML, de Wit J, Savas JN, Comoletti D, Otto-Hitt S, Yates JR, and Ghosh A (2012). FLRT proteins are endogenous latrophilin ligands and regulate excitatory synapse development. Neuron 73, 903–910. 10.1016/j.neuron.2012.01.018. [PubMed: 22405201]
35. Yamagishi S, Hampel F, Hata K, Del Toro D, Schwark M, Kvachnina E, Bastmeyer M, Yamashita T, Tarabykin V, Klein R, and Egea J (2011). FLRT2 and FLRT3 act as repulsive guidance cues for Unc5-positive neurons. EMBO J. 30, 2920–2933. 10.1038/emboj.2011.189. [PubMed: 21673655]
36. Ranaivoson FM, Liu Q, Martini F, Bergami F, von Daake S, Li S, Lee D, Demeler B, Hendrickson WA, and Comoletti D (2015). Structural and Mechanistic Insights into the Latrophilin3-FLRT3 Complex that Mediates Glutamatergic Synapse Development. Structure (London, England : 1993) 23, 1665–1677. 10.1016/j.str.2015.06.022. [PubMed: 26235031]
37. Lu YC, Nazarko OV, Sando R, Salzman GS, Li N-S, Südhof TC, and Araç D (2015). Structural Basis of Latrophilin-FLRT-UNC5 Interaction in Cell Adhesion. Structure (London, England : 1993) 23, 1678–1691. 10.1016/j.str.2015.06.024. [PubMed: 26235030]
38. Jackson VA, del Toro D, Carrasquero M, Roversi P, Harlos K, Klein R, and Seiradake E (2015). Structural basis of latrophilin-FLRT interaction. Structure (London, England : 1993) 23, 774–781. 10.1016/j.str.2015.01.013. [PubMed: 25728924]
39. Sando R, Jiang X, and Südhof TC (2019). Latrophilin GPCRs direct synapse specificity by coincident binding of FLRTs and teneurins. Science (New York, N.Y.) 363, eaav7969. 10.1126/science.aav7969. [PubMed: 30792275]
40. del Toro D, Carrasquero-Ordaz MA, Chu A, Ruff T, Shahin M, Jackson VA, Chavent M, Berbeira-Santana M, Seyit-Bremer G, Brignani S, et al. (2020). Structural Basis of Teneurin-Latrophilin Interaction in Repulsive Guidance of Migrating Neurons. Cell 180, 323–339.e319. 10.1016/j.cell.2019.12.014. [PubMed: 31928845]
41. Famiglietti EV, and Sundquist SJ (2010). Development of excitatory and inhibitory neurotransmitters in transitory cholinergic neurons, starburst amacrine cells, and GABAergic amacrine cells of rabbit retina, with implications for previsual and visual development of retinal ganglion cells. Vis Neurosci 27, 19–42. 10.1017/S0952523810000052. [PubMed: 20392300]
42. Yan W, Laboulaye MA, Tran NM, Whitney IE, Benhar I, and Sanes JR (2020). Mouse Retinal Cell Atlas: Molecular Identification of over Sixty Amacrine Cell Types. J. Neurosci. 40, 5177–5195. 10.1523/JNEUROSCI.0471-20.2020. [PubMed: 32457074]
43. Furuta Y, Lagutin O, Hogan BL, and Oliver GC (2000). Retina- and ventral forebrain-specific Cre recombinase activity in transgenic mice. Genesis 26, 130–132. [PubMed: 10686607]
44. Trenholm S, Johnson K, Li X, Smith RG, and Awatramani GB (2011). Parallel mechanisms encode direction in the retina. Neuron 71, 683–694. 10.1016/j.neuron.2011.06.020. [PubMed: 21867884]
45. Huberman AD, Wei W, Elstrott J, Stafford BK, Feller MB, and Barres BA (2009). Genetic identification of an On-Off direction-selective retinal ganglion cell subtype reveals a layer-specific subcortical map of posterior motion. Neuron 62, 327–334. 10.1016/j.neuron.2009.04.014. [PubMed: 19447089]
46. Kay JN, De la Huerta I, Kim I-J, Zhang Y, Yamagata M, Chu MW, Meister M, and Sanes JR (2011). Retinal ganglion cells with distinct directional preferences differ in molecular identity, structure, and central projections. J. Neurosci. 31, 7753–7762. 10.1523/JNEUROSCI.0907-11.2011. [PubMed: 21613488]
47. Kim D, and Ackerman SL (2011). The UNC5C Netrin Receptor Regulates Dorsal Guidance of Mouse Hindbrain Axons. J. Neurosci. 31, 2167–2179. 10.1523/jneurosci.5254-10.2011. [PubMed: 21307253]
48. Ackerman SL, Kozak LP, Przyborski SA, Rund LA, Boyer BB, and Knowles BB (1997). The mouse rostral cerebellar malformation gene encodes an UNC-5-like protein. Nature 386, 838–842. 10.1038/386838a0. [PubMed: 9126743]
49. Fleitas C, Marfull-Oromi P, Chauhan D, Del Toro D, Peguera B, Zammou B, Rocandio D, Klein R, Espinet C, and Egea J (2021). FLRT2 and FLRT3 Cooperate in Maintaining the Tangential Migratory Streams of Cortical Interneurons during Development. J Neurosci 41, 7350–7362. 10.1523/JNEUROSCI.0380-20.2021. [PubMed: 34301831]

50. Mani A, Yang X, Zhao T, Leyrer ML, Schreck D, and Berson DM (2022). A retinal circuit that vetoes optokinetic responses to fast visual motion. bioRxiv, 2021.2010.2031.466688. 10.1101/2021.10.31.466688.

51. Della Santina L, Inman DM, Lupien CB, Horner PJ, and Wong ROL (2013). Differential progression of structural and functional alterations in distinct retinal ganglion cell types in a mouse model of glaucoma. J. Neurosci. 33, 17444–17457. 10.1523/JNEUROSCI.5461-12.2013. [PubMed: 24174678]

52. Tiriac A, Bistrong K, Pitcher MN, Tworig JM, and Feller MB (2022). The influence of spontaneous and visual activity on the development of direction selectivity maps in mouse retina. Cell Rep. 38, 110225. 10.1016/j.celrep.2021.110225. [PubMed: 35021080]

53. Wei W, Hamby AM, Zhou K, and Feller MB (2011). Development of asymmetric inhibition underlying direction selectivity in the retina. Nature 469, 402–406. 10.1038/nature09600. [PubMed: 21131947]

54. Yonehara K, Balint K, Noda M, Nagel G, Bamberg E, and Roska B (2011). Spatially asymmetric reorganization of inhibition establishes a motion-sensitive circuit. Nature 469, 407–410. 10.1038/nature09711. [PubMed: 21170022]

55. Fisher LJ (1979). Development of synaptic arrays in the inner plexiform layer of neonatal mouse retina. J. Comp. Neurol. 187, 359–372. 10.1002/cne.901870207. [PubMed: 489784]

56. Lefebvre JL, Kostadinov D, Chen WV, Maniatis T, and Sanes JR (2012). Protocadherins mediate dendritic self-avoidance in the mammalian nervous system. Nature 488, 517–521. 10.1038/nature11305. [PubMed: 22842903]

57. Kim I-J, Zhang Y, Meister M, and Sanes JR (2010). Laminar restriction of retinal ganglion cell dendrites and axons: subtype-specific developmental patterns revealed with transgenic markers. J. Neurosci. 30, 1452–1462. 10.1523/JNEUROSCI.4779-09.2010. [PubMed: 20107072]

58. Leyva-Díaz E, del Toro D, Menal MJ, Cambray S, Susín R, Tessier-Lavigne M, Klein R, Egea J, and López-Bendito G (2014). FLRT3 is a Robo1-interacting protein that determines Netrin-1 attraction in developing axons. Current biology : CB 24, 494–508. 10.1016/j.cub.2014.01.042. [PubMed: 24560577]

59. Kay JN, Chu MW, and Sanes JR (2012). MEGF10 and MEGF11 mediate homotypic interactions required for mosaic spacing of retinal neurons. Nature 483, 465–469. 10.1038/nature10877. [PubMed: 22407321]

60. Rheaume BA, Jereen A, Bolisetty M, Sajid MS, Yang Y, Renna K, Sun L, Robson P, and Trakhtenberg EF (2018). Single cell transcriptome profiling of retinal ganglion cells identifies cellular subtypes. Nature Communications 9. 10.1038/s41467-018-05134-3.

61. Tran NM, Shekhar K, Whitney IE, Jacobi A, Benhar I, Hong G, Yan W, Adiconis X, Arnold ME, Lee JM, et al. (2019). Single-Cell Profiles of Retinal Ganglion Cells Differing in Resilience to Injury Reveal Neuroprotective Genes. Neuron 104, 1039–1055.e1012. 10.1016/j.neuron.2019.11.006. [PubMed: 31784286]

62. Scheiffele P, Fan J, Choih J, Fetter R, and Serafini T (2000). Neuroligin expressed in nonneuronal cells triggers presynaptic development in contacting axons. Cell 101, 657–669. 10.1016/s0092-8674(00)80877-6. [PubMed: 10892652]

63. Sanes JR, and Zipursky SL (2010). Design principles of insect and vertebrate visual systems. Neuron 66, 15–36. 10.1016/j.neuron.2010.01.018. [PubMed: 20399726]

64. Xie X, Tabuchi M, Brown MP, Mitchell SP, Wu MN, and Kolodkin AL (2017). The laminar organization of the Drosophila ellipsoid body is semaphorin-dependent and prevents the formation of ectopic synaptic connections. eLife 6, e25328. 10.7554/eLife.25328. [PubMed: 28632130]

65. Murcia-Belmonte V, Coca Y, Vegar C, Negueruela S, de Juan Romero C, Valiño AJ, Sala S, DaSilva R, Kania A, Borrell V, et al. (2019). A Retino-retinal Projection Guided by Unc5c Emerged in Species with Retinal Waves. Current biology : CB 29, 1149–1160.e1144. 10.1016/j.cub.2019.02.052. [PubMed: 30905607]

66. Yamada M, Fujita Y, Hayano Y, Hayakawa H, Baba K, Mochizuki H, and Yamashita T (2019). Increased Expression of Fibronectin Leucine-Rich Transmembrane Protein 3 in the Dorsal Root Ganglion Induces Neuropathic Pain in Rats. J Neurosci 39, 7615–7627. 10.1523/JNEUROSCI.0295-19.2019. [PubMed: 31346030]

67. Del Toro D, Ruff T, Cederfjäll E, Villalba A, Seyit-Bremer G, Borrell V, and Klein R (2017). Regulation of Cerebral Cortex Folding by Controlling Neuronal Migration via FLRT Adhesion Molecules. Cell 169, 621–635.e616. 10.1016/j.cell.2017.04.012. [PubMed: 28475893]

68. Ando T, Tai-Nagara I, Sugiura Y, Kusumoto D, Okabayashi K, Kido Y, Sato K, Saya H, Navankasattusas S, Li DY, et al. (2022). Tumor-specific interendothelial adhesion mediated by FLRT2 facilitates cancer aggressiveness. J. Clin. Invest. 132. 10.1172/JCI153626.

69. Khani M, Gibbons E, Bras J, and Guerreiro R (2022). Challenge accepted: uncovering the role of rare genetic variants in Alzheimer’s disease. Mol Neurodegener 17, 3. 10.1186/s13024-021-00505-9. [PubMed: 35000612]

70. Schroeder A, Vanderlinden J, Vints K, Ribeiro LF, Vennekens KM, Gounko NV, Wierda KD, and de Wit J (2018). A Modular Organization of LRR Protein-Mediated Synaptic Adhesion Defines Synapse Identity. Neuron 99, 329–344.e327. 10.1016/j.neuron.2018.06.026. [PubMed: 29983322]

71. El-Quessny M, Maanum K, and Feller MB (2020). Visual Experience Influences Dendritic Orientation but Is Not Required for Asymmetric Wiring of the Retinal Direction Selective Circuit. Cell Rep. 31, 107844. 10.1016/j.celrep.2020.107844. [PubMed: 32610144]

72. Wong ROL, and Ghosh A (2002). Activity-dependent regulation of dendritic growth and patterning. Nature reviews. Neuroscience 3, 803–812. 10.1038/nrn941. [PubMed: 12360324]

73. Ing-Esteves S, and Lefebvre JL (2021). Time-Lapse Imaging of Neuronal Arborization using Sparse Adeno-Associated Virus Labeling of Genetically Targeted Retinal Cell Populations. J Vis Exp. 10.3791/62308.

74. Cline H, and Haas K (2008). The regulation of dendritic arbor development and plasticity by glutamatergic synaptic input: a review of the synaptotrophic hypothesis. The Journal of physiology 586, 1509–1517. 10.1113/jphysiol.2007.150029. [PubMed: 18202093]

75. Niell CM, Meyer MP, and Smith SJ (2004). In vivo imaging of synapse formation on a growing dendritic arbor. Nat. Neurosci. 7, 254–260. 10.1038/nn1191. [PubMed: 14758365]

76. Takeo YH, Shuster SA, Jiang L, Hu MC, Luginbuhl DJ, Rulicke T, Contreras X, Hippenmeyer S, Wagner MJ, Ganguli S, and Luo L (2021). GluD2- and Cbln1-mediated competitive interactions shape the dendritic arbors of cerebellar Purkinje cells. Neuron 109, 629–644 e628. 10.1016/j.neuron.2020.11.028. [PubMed: 33352118]

77. Lohmann C, Myhr KL, and Wong ROL (2002). Transmitter-evoked local calcium release stabilizes developing dendrites. Nature 418, 177–181. 10.1038/nature00850. [PubMed: 12110889]

78. Südhof TC (2018). Towards an Understanding of Synapse Formation. Neuron. 10.1016/j.neuron.2018.09.040.

79. Ruff T, Peters C, Matsumoto A, Ihle SJ, Morales PA, Gaitanos L, Yonehara K, Del Toro D, and Klein R (2021). FLRT3 Marks Direction-Selective Retinal Ganglion Cells That Project to the Medial Terminal Nucleus. Front Mol Neurosci 14, 790466. 10.3389/fnmol.2021.790466. [PubMed: 34955746]

80. Shekhar K, Whitney IE, Butrus S, Peng YR, and Sanes JR (2022). Diversification of multipotential postmitotic mouse retinal ganglion cell precursors into discrete types. Elife 11. 10.7554/eLife.73809.

81. Goetz J, Jessen ZF, Jacobi A, Mani A, Cooler S, Greer D, Kadri S, Segal J, Shekhar K, Sanes JR, and Schwartz GW (2022). Unified classification of mouse retinal ganglion cells using function, morphology, and gene expression. Cell Rep. 40, 111040. 10.1016/j.celrep.2022.111040. [PubMed: 35830791]

82. Ippolito DM, and Eroglu C (2010). Quantifying Synapses: an Immunocytochemistry-based Assay to Quantify Synapse Number. Journal of Visualized Experiments. 10.3791/2270.

83. Savage JT, Ramirez J, Risher WC, Irala D, and Eroglu C (2023). SynBot: An open-source image analysis software for automated quantification of synapses. bioRxiv. 10.1101/2023.06.26.546578.

84. Jiang W, Gong J, Rong Y, and Yang X (2019). A new co-culture method for identifying synaptic adhesion molecules involved in synapse formation. Biophysics Reports 5, 91–97. 10.1007/s41048-019-0084-4.

85. Modzelewski AJ, Chen S, Willis BJ, Lloyd KCK, Wood JA, and He L (2018). Efficient mouse genome engineering by CRISPR-EZ technology. Nat Protoc 13, 1253–1274. 10.1038/nprot.2018.012. [PubMed: 29748649]

86. Peng BY, Wang Q, Luo YH, He JF, Tan T, and Zhu H (2018). A novel and quick PCR-based method to genotype mice with a leptin receptor mutation (db/db mice). Acta Pharmacol Sin 39, 117–123. 10.1038/aps.2017.52. [PubMed: 28748911]

87. Manders EM, Stap J, Brakenhoff GJ, van Driel R, and Aten JA (1992). Dynamics of three-dimensional replication patterns during the S-phase, analysed by double labelling of DNA and confocal microscopy. J. Cell Sci. 103 *(* Pt 3*)*, 857–862. 10.1242/jcs.103.3.857. [PubMed: 1478975]

88. Schindelin J, Arganda-Carreras I, Frise E, Kaynig V, Longair M, Pietzsch T, Preibisch S, Rueden C, Saalfeld S, Schmid B, et al. (2012). Fiji: an open-source platform for biological-image analysis. Nat. Methods 9, 676–682. 10.1038/nmeth.2019. [PubMed: 22743772]

89. Stuart T, Butler A, Hoffman P, Hafemeister C, Papalexi E, Mauck WM, Hao Y, Stoeckius M, Smibert P, and Satija R (2019). Comprehensive Integration of Single-Cell Data. Cell 177, 1888–1902.e1821. 10.1016/j.cell.2019.05.031. [PubMed: 31178118]

90. Wang Y, Cao Y, Hays CL, Laboute T, Ray TA, Guerrero-Given D, Ahuja AS, Patil D, Rivero O, Kamasawa N, et al. (2021). Adhesion GPCR Latrophilin 3 regulates synaptic function of cone photoreceptors in a trans-synaptic manner. Proc. Natl. Acad. Sci. USA 118. 10.1073/pnas.2106694118.

91. Koh S, Chen WJ, Dejneka NS, Harris IR, Lu B, Girman S, Saylor J, Wang S, and Eroglu C (2018). Subretinal Human Umbilical Tissue-Derived Cell Transplantation Preserves Retinal Synaptic Connectivity and Attenuates Müller Glial Reactivity. The Journal of Neuroscience 38, 2923–2943. 10.1523/JNEUROSCI.1532-17.2018. [PubMed: 29431645]

92. Longair MH, Baker DA, and Armstrong JD (2011). Simple Neurite Tracer: open source software for reconstruction, visualization and analysis of neuronal processes. Bioinformatics 27, 2453–2454. 10.1093/bioinformatics/btr390. [PubMed: 21727141]

93. El-Quessny M, and Feller MB (2021). Dendrite Morphology Minimally Influences the Synaptic Distribution of Excitation and Inhibition in Retinal Direction-Selective Ganglion Cells. eNeuro 8. 10.1523/ENEURO.0261-21.2021.

94. Schnütgen F, Doerflinger N, Calléja C, Wendling O, Chambon P, and Ghyselinck NB (2003). A directional strategy for monitoring Cre-mediated recombination at the cellular level in the mouse. Nat. Biotechnol. 21, 562–565. 10.1038/nbt811. [PubMed: 12665802]

Highlights

- Retinal dendrites expressing FLRT2 and UNC5C exhibit mutual avoidance
- FLRT2-UNC5 binding promotes elimination of mistargeted dendrite branches
- Mistargeted dendrites form inappropriate synapses when FLRT2-UNC5 binding is lost
- UNC5 binding sculpts FLRT2$^+$ dendrites by occluding FLRT2-latrophilin adhesion

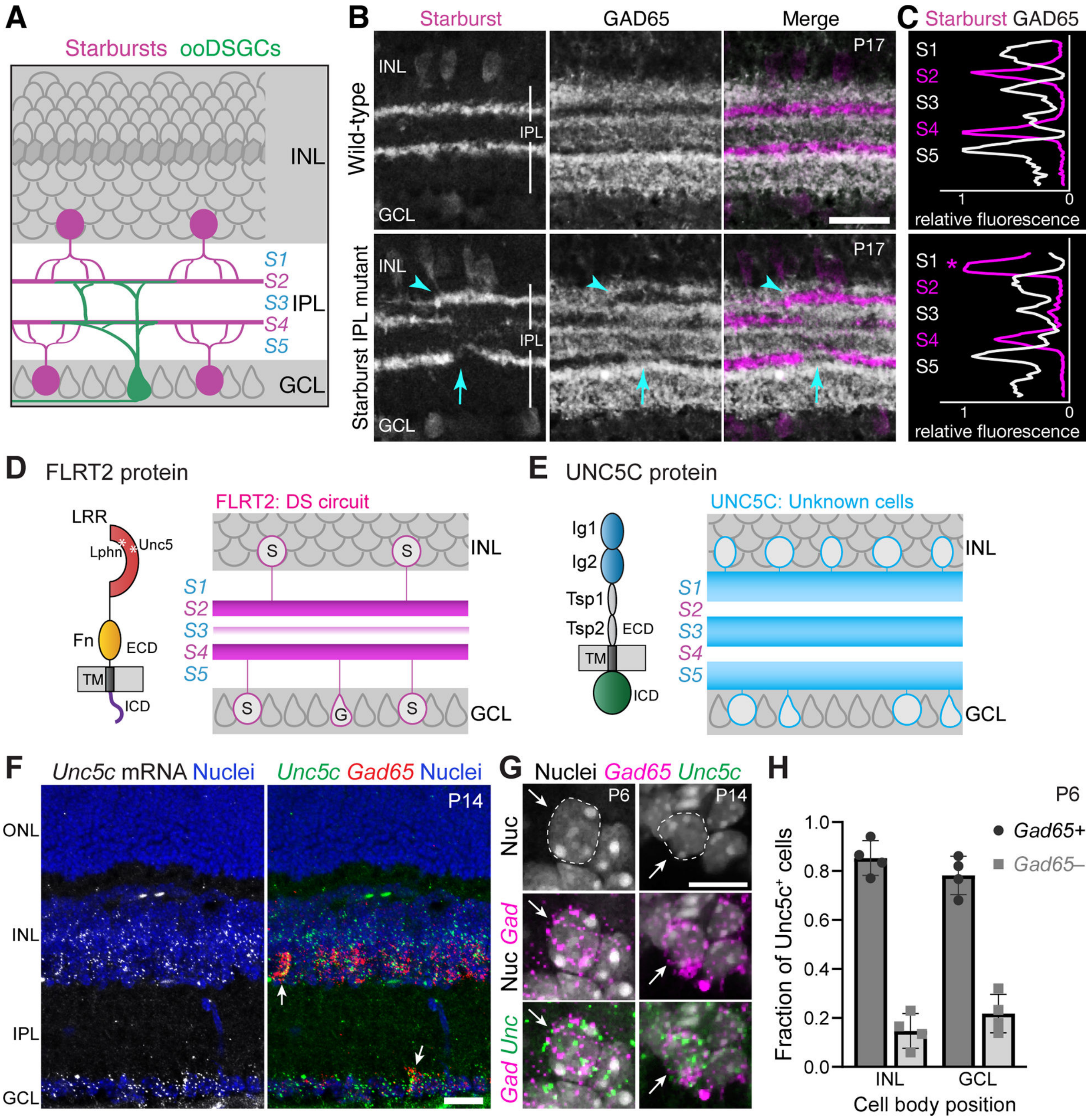

Figure 1: GAD65$^+$ amacrine cells express UNC5C and exhibit mutual exclusion with DS circuit dendrites

A. Schematic of mouse retina (cross-section view) showing DS circuit cell types studied here. OFF starburst amacrine cells in inner nuclear layer (INL) project to inner plexiform layer (IPL) sublayer S2; ON starbursts in ganglion cell layer (GCL) project to S4. ON-OFF direction-selective ganglion cell (ooDSGC) dendrites cofasciculate with starburst dendrites in both sublayers. Amacrine cell dendrites contain both pre- and postsynaptic sites; starburst cells release GABA and acetylcholine onto ooDSGCs.

B,C. Perturbation of starburst dendritic targeting using *Megf10* mutants[26] reveals mutual repulsion with GAD65$^+$ amacrine cell dendrites. B: Retinal cross-sections stained with anti-ChAT (starburst marker) and anti-GAD65. C: Representative profile plots quantifying ChAT and GAD65 fluorescence across IPL. Controls (top; *Megf10*$^{flox/flox}$; no Cre, n = 4) exhibit sharp boundaries between ChAT$^+$ and GAD65$^+$ IPL strata. In mutants (bottom, n = 4, *Six3-Cre; Megf10*$^{flox/flox}$), starburst dendrites enter GAD65$^+$ IPL regions, displacing GAD65 arbors (B, arrowheads; C, asterisk). Starburst dendrites also sporadically fail to innervate regions within S2 and S4; GAD65$^+$ arbors invade these regions (arrows).

D,E. Schematics of FLRT2 and UNC5C protein structure (left panels) and protein localization within IPL as per our previous study[30] (right panels). FLRT2 is present in S2/S4 due to expression by ooDSGCs (G) and starburst cells (S). FLRT2 also localizes to S3. UNC5C is absent from S2 and S4 (E). LRR, leucine-rich repeat; Fn, Fibronectin-like domain; TM, transmembrane domain; ECD, extracellular domain; ICD, intracellular domain. Ig, immunoglobulin; Tsp, thrombospondin domains. FLRT2 binding sites for latrophilins (Lphn) and UNC5s are indicated.

F,G. In situ hybridization for *Unc5c* and Gad65 (gene symbol *Gad2*) to mark GABAergic amacrine cells. Blue, Hoechst nuclear counterstain. F: Prominent *Unc5c* expression at P15 in GCL and INL, including amacrine subregion of INL (marked by Gad65). *Unc5c* labels a subset of Gad65$^+$ amacrine cells in the INL and displaced Gad65$^+$ amacrine cells in GCL (arrows). RGCs (Gad65-negative GCL cells) also express *Unc5c*. Expression is similar at P6 (Supplemental Fig. S1A). G: Representative images of Gad65$^+$*Unc5c*$^+$ double-positive cells.

H. Fraction of *Unc5c*$^+$ cells co-expressing Gad65, quantified from images similar to F,G. Most *Unc5*$^+$ cells in GCL are GABAergic displaced amacrines rather than RGCs. N = 4 animals.

Scale bars, 10 μm (B,G); 20 μm (F). Also see Supplemental Fig. S1.

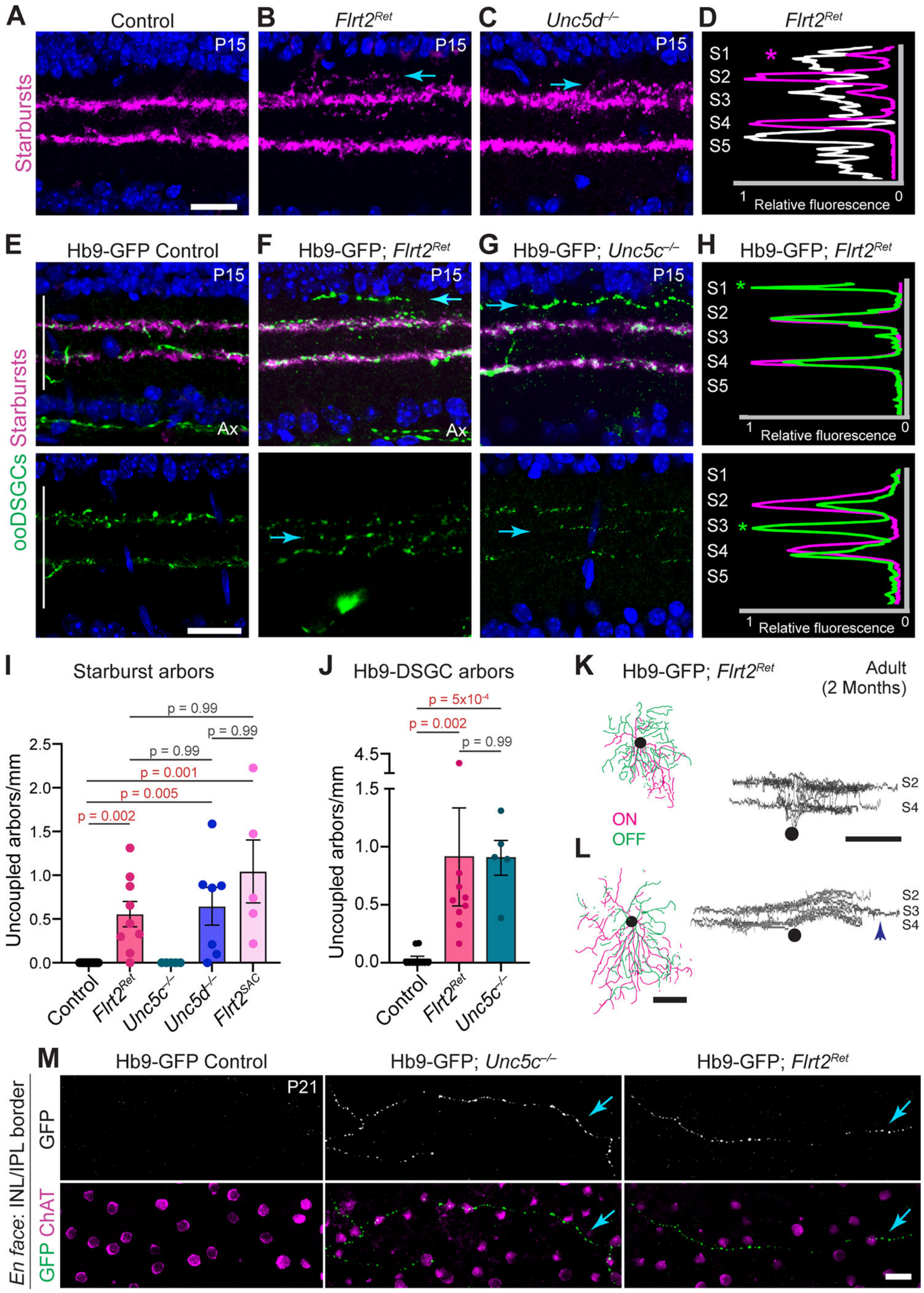

Figure 2: Starburst and ooDSGC laminar targeting errors in *Flrt2* and *Unc5* mutants.

A-D. Starburst dendrite targeting errors in *Flrt2*^{Ret} and *Unc5d* mutants. A-C, representative cross-section images; D, fluorescence profile plots (white, anti-GAD65). Magenta, anti-VAChT. Arrows (A-C) and asterisks (D) mark ectopic starburst dendrites in S1.

E-H. Hb9-ooDSGC dendrite targeting errors in *Flrt2*^{Ret} and *Unc5c* mutants. Magenta, anti-VAChT; green, anti-GFP (labeling ooDSGCs). Vertical bar, IPL neuropil. Arrows (E-G) and asterisks (H) mark ectopic ooDSGC arbors in S1 (top row) or S3 (bottom row) that are uncoupled from starburst arbors. Ax, GFP$^+$ axons within nerve fiber layer. Blue, Hoechst nuclear counterstain.

I,J: Summary of starburst (I) and ooDSGC (J) laminar targeting errors. ooDSGC phenotype strength was similar in *Flrt2*^{Ret} and *Unc5c*$^{-/-}$. Starburst phenotype strength was similar in *Flrt2* whole-retina (*Flrt2*^{Ret}) and starburst-specific (*Flrt2*^{SAC}) mutants, as well as *Unc5d*$^{-/-}$. Statistics (I), Kruskal-Wallis test (main effect $p=1.6\times10^{-5}$) with Dunn's post-hoc test. Sample sizes (number of animals): littermate controls n = 9, *Flrt2*^{Ret} n = 9, *Unc5c*$^{-/-}$ n = 5; *Unc5d*$^{-/-}$ n = 7; *Flrt2*^{SAC} n = 5. Statistics (J), Kruskal-Wallis test (main effect $p=9.2\times10^{-5}$) with Dunn's post-hoc test. Sample sizes (number of animals): littermate controls n = 11 (n = 6 *Flrt2*^{WT}; n = 5 *Unc5c*$^{+/+}$), *Flrt2*^{Ret} n = 9, *Unc5c*$^{-/-}$ n = 5. Error bars, S.E.M. P-values (shown on graph) were corrected for multiple comparisons.

K,L. Single cell reconstructions of dye-filled Hb9-ooDSGCs from *Flrt2*^{Ret} mutants. F, normally-stratified ooDSGC; G, ooDSGC with ectopic S3 dendritic arbor. n = 3/12 filled cells exhibited ectopic arbors.

M. En-face view of ectopic ooDSGC arbors in retinal wholemounts. To depict S1 IPL sublayer, confocal images were acquired at plane of IPL/INL border. Hb9-GFP$^+$ arbors do not project to this location in wild-type retina (left) but are readily observed in both *Unc5c*$^{-/-}$ and *Flrt2*^{Ret} mutants (arrows).

Scale bars, 20 μm (A-C, E-G, M); 100 μm (K,L). Error bars, S.E.M. Also see Supplemental Figs. S2–S5.

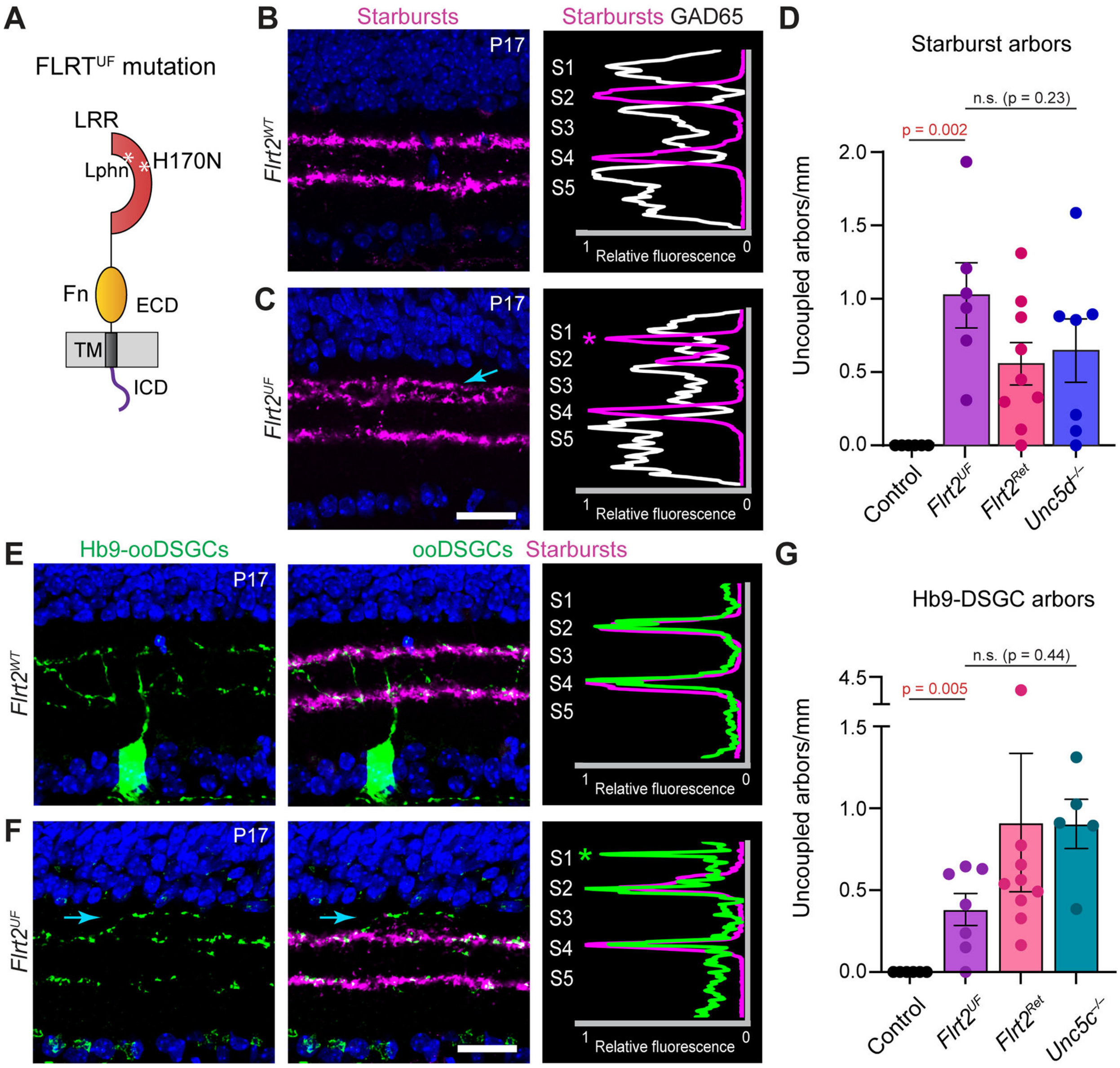

Figure 3: Abolishing FLRT2-UNC5 binding disrupts DS circuit laminar targeting

A. FLRT2^{UF} mutant protein. H170N mutation introduces N-glycosylation site within LRR domain at UNC5 binding surface. LPHN binding site is unaffected. Abbreviations, see Fig. 1D,E.

B,C. Starburst laminar targeting errors in homozygous *Flrt2*^{UF} mutants. Left, VAChT immunostaining; right, profile plots (VAChT and GA65 fluorescence). Unlike controls (B), mutants (C) exhibit ectopic dendrites within S1 (arrow, asterisk).

D. Summary of starburst laminar errors in *Flrt2*^{UF} mutants and *Flrt2*^{WT} littermate controls. Statistics, two-tailed Mann-Whitney test; sample sizes n = 6 littermate controls; n = 6 *Flrt2*^{UF} mutants. For comparison, *Flrt2*^{Ret} and *Unc5d*$^{-/-}$ mutant data are replotted from Fig. 2. There was no significant difference in error frequency between *Flrt2*^{UF} and the other two mutants (one-way ANOVA, F(2, 19) = 1.60; n.s., not significant).

E,F. ooDSGC dendrite targeting errors are observed in *Flrt2*^{UF} mutants (F) but not littermate controls (E). Arrow, ectopic ooDSGC arbor within S1.

G. Summary of Hb9-ooDSGC laminar errors in *Flrt2*^{UF} mutants and *Flrt2*^{WT} littermate controls. Statistics, two-tailed Mann-Whitney test; sample sizes n = 6 littermate controls; n = 7 *Flrt2*^{UF} mutants. For comparison, *Flrt2*^{Ret} and *Unc5c*$^{-/-}$ mutant data are replotted from Fig. 2. There is a trend towards fewer errors in *Flrt2*^{UF} compared to the other two mutants but the difference was not significant (one-way ANOVA, F(2, 18) = 0.85).

Scale bars, 20 μm. Error bars (D,G), S.E.M.

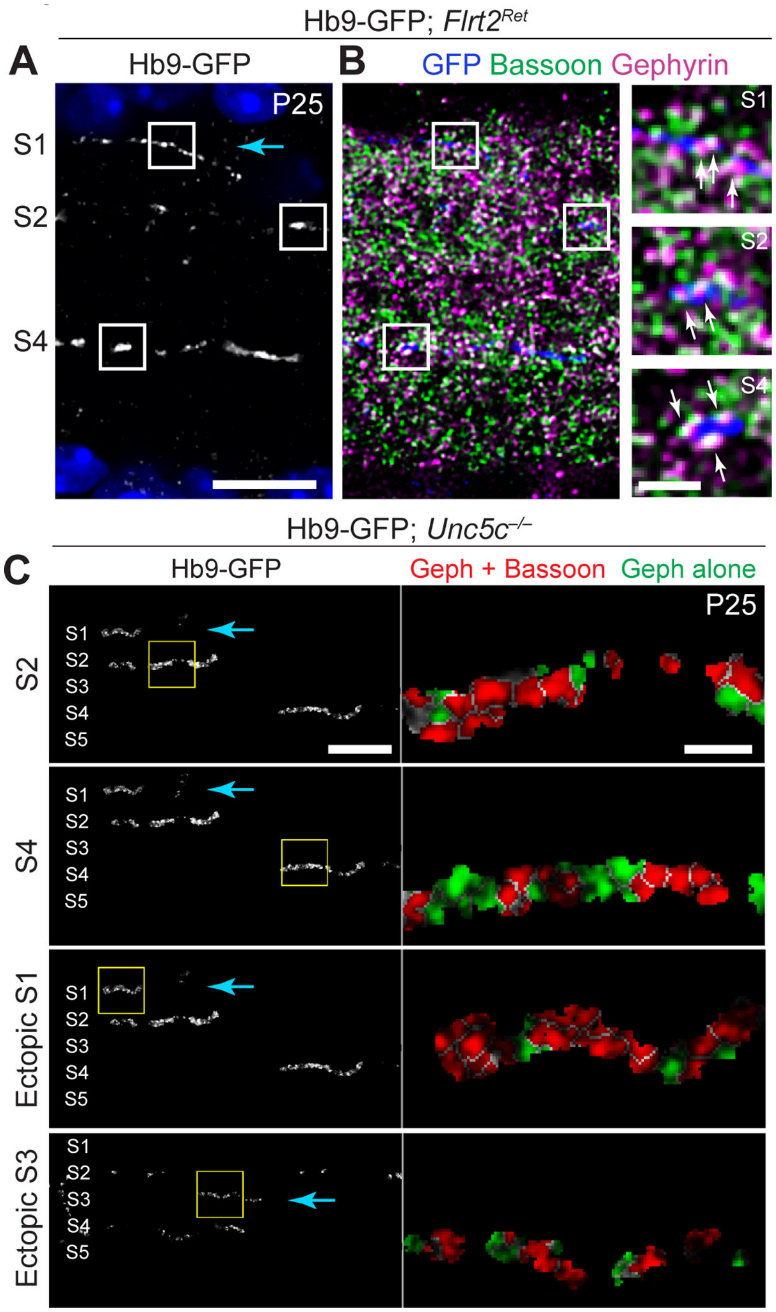

Figure 4: Mistargeted ooDSGC arbors in *Flrt2*^{Ret} and *Unc5c* mutants receive inhibitory synapses.

A-**B**. Inhibitory synapse labeling in P25 *Hb9-GFP*; *Flrt2*^{Ret} mutant (single optical slice from representative confocal stack). A, GFP channel alone; blue arrow, ectopic ooDSGC arbor. B, GFP overlay with bassoon and gephyrin. Boxed regions are shown at high magnification (B, right). White signals indicate putative synaptic sites where bassoon and gephyrin puncta overlap. Putative synapses (white arrows) are observed along ooDSGC dendrites in normal DS circuit sublayers (S2, S4) and ectopic sublayers (S1).

C. Semi-automated unbiased synapse identification in *Hb9-GFP*; *Unc5c*$^{-/-}$ mutant. ObjectFinder software was used to analyze images similar to B. Left, GFP channel 3D mask, demarcating ooDSGC dendrites. Right, segmentation of paired bassoon-gephyrin synaptic structures (red) within GFP mask. Synapses are evident along ectopic arbors (S1, S3, blue arrows), similar to normally targeted arbors (S2, S4). Green, non-synaptic gephyrin signal (i.e. without bassoon co-localization). Images are representative of n = 4 *Unc5c*$^{-/-}$ and n = 4 *Flrt2*^{Ret} animals.

Scale bars: 10 μm (A; B, left); 2 μm (B, right) 20 μm (C, left); 5 μm (D, right). Also see Supplemental Fig. S5D,E.

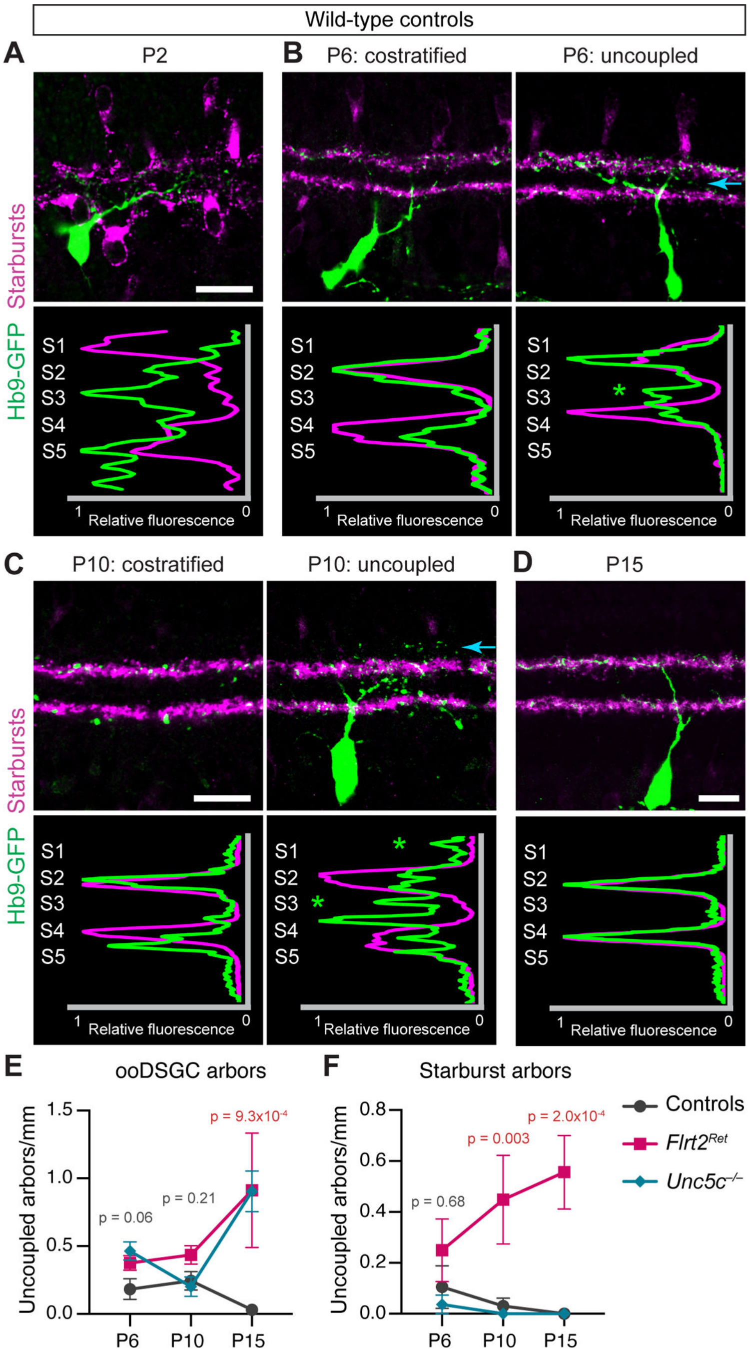

Figure 5: Refinement of DS circuit laminar targeting between P6 and P15.

A-D. Developmental timecourse showing starburst and Hb9-ooDSGC IPL projections at specified ages. All images from wild-type animals (i.e. *Flrt2*$^{+/+}$; *Unc5c*$^{+/+}$); for mutant images, see Supplemental Fig. S6. At P2 (A), starburst IPL strata are evident; ooDSGC arbors are not yet stratified. At P6 (B) and P10 (C), both cell types are largely co-stratified although uncoupled ooDSGC arbors outside S2/S4 are evident (right panels; arrows). By P15 (D) all ooDSGC dendrites are coupled with starburst scaffold.

E,F. Quantification of ooDSGC (E) and starburst (F) laminar errors in *Flrt2*^{Ret} mutants; *Unc5c*$^{-/-}$ mutants; and wild-type littermate controls. P15 data are replotted from Fig. 2 to facilitate comparisons with younger ages. Differences between mutant and controls do not arise until P15 (ooDSGCs) or P10 (starbursts). Statistics (E,F): Kruskal-Wallis test; P-values on graph are for main effect of genotype at each age. Sample sizes: P6 control n = 7; P6 *Flrt2*^{Ret} n = 8; P6 *Unc5c*$^{-/-}$ n = 4; P10 control n = 8; P10 *Flrt2*^{Ret} n = 4 (E) or n = 5 (F); P10 *Unc5c*$^{-/-}$ n = 6.

Scale bars, 20 μm (bar in A also applies to B). Error bars, S.E.M. Also see Supplemental Fig. S6.

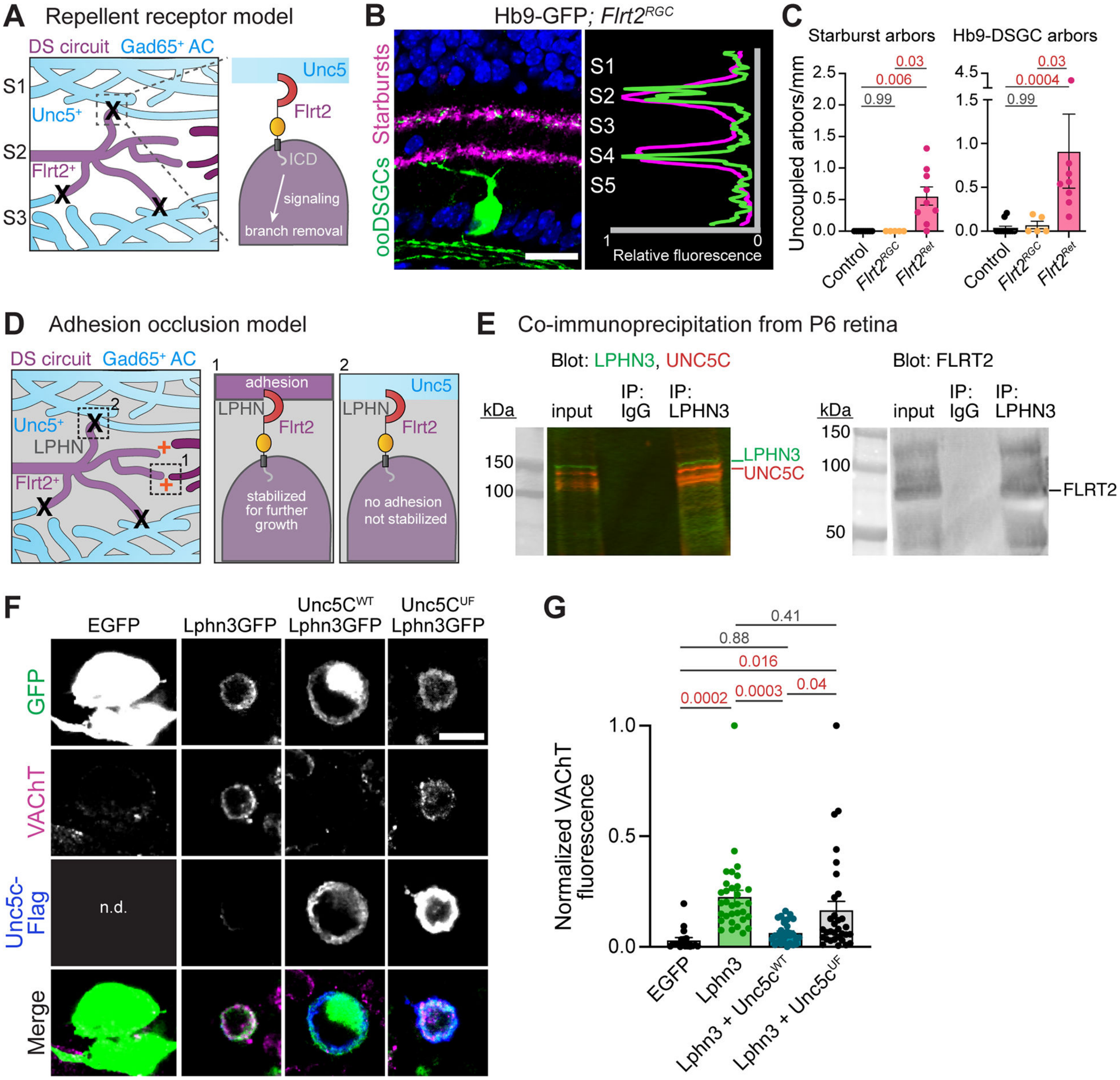

Figure 6: UNC5s function by occluding FLRT-LPHN adhesion

A. Illustration of repellent receptor model: FLRT2 transduces repulsive signals upon UNC5 binding, driving elimination of mistargeted dendrite branches (X). Model predicts cell-autonomous requirement for FLRT2 within ooDSGCs.

B,C: Deletion of *Flrt2* from RGCs (*Flrt2*^{RGC} mutants) rules out repellent receptor model. B, Representative image (left) and profile plots (right) showing normal dendrite targeting of Hb9-ooDSGCs (anti-GFP) and starbursts (anti-VAChT) in *Flrt2*^{RGC} mutants. C: quantification of mistargeted dendrites. Sample sizes: littermate controls, n = 9; *Flrt2*^{RGC} n = 5. For comparison, *Flrt2*^{Ret} data are replotted from Fig. 2. Statistics, Kruskal-Wallace test with post-hoc Dunn's test. P-values were corrected for multiple comparisons.

D. Illustration of adhesion-occlusion model: LPHN protein (gray) localizes throughout IPL, including starburst and ooDSGC dendrites; UNC5s are in non-DS sublayers. Dendritic contacts among DS circuit neurons are stabilized (orange +) by transcellular reciprocal FLRT2-LPHN adhesion (inset 1). Contacts with inappropriate partners also result in FLRT2-LPHN binding, but these are not stabilized (X) due to presence of UNC5 which occludes FLRT2-LPHN adhesion (inset 2).

E. Co-immunoprecipitation indicates LPHN3-UNC5C-FLRT2 complex is present in P6 retina. UNC5C (left) and FLRT2 (right) are enriched in LPHN3 pull-down condition compared to input lysates or to IgG pull-down control. Upper FLRT2 band (just below 150 kDa) likely corresponds to FLRT2 dimer.

F,G. Adhesion assay using primary retinal neurons co-cultured with HEK cells. F, representative images of VAChT$^+$ starburst arbors associating with HEK cells transfected as indicated; G. quantification of VAChT fluorescence surrounding HEK cells. Starburst arbors encircle HEK cells transfected with LPHN3-GFP, but not GFP alone. Starburst-LPHN3 adhesion is blocked by co-transfection of flag-tagged wild-type (WT) UNC5C, but not UNC5C^{UF} mutant that cannot bind FLRTs. n.d., staining was not performed. Statistics: One way ANOVA with Tukey’s post-hoc test. P-values were corrected for multiple comparisons. Sample sizes (number of cells): n = 18 EGFP; n = 32 Lphn3 alone; n = 31 Lphn3+Unc5c^{WT}; n = 32 Lphn3+Unc5c^{UF}. Data from three independent culture experiments.

Scale bars, 20 μm (B); 10 μm (F). Error bars, S.E.M. Also see Supplemental Fig. S6.

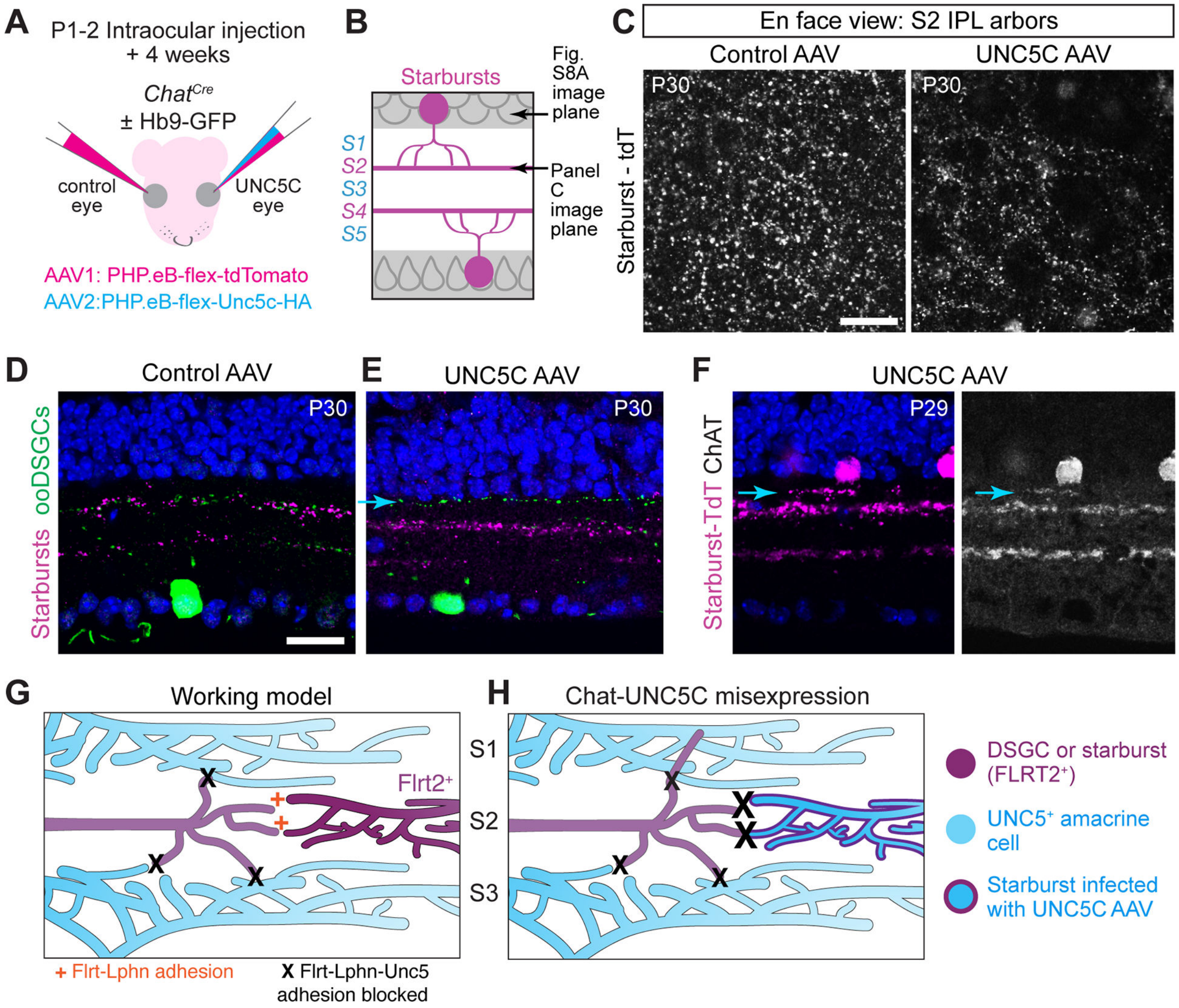

Figure 7: Misexpression of UNC5C in starburst cells induces DS circuit laminar targeting errors.

A. Strategy for starburst-specific flex-switch AAV expression in *Chat*^{Cre} mice. PHP.eB, AAV serotype.

B. Illustration showing confocal imaging planes used for wholemount analysis of AAV-infected retinas (C, Supplemental Fig. S7A).

C. Starburst dendritic density is diminished by UNC5C misexpression. En-face views of tdTomato (tdT)$^{+}$ OFF starburst dendrites in retinal wholemounts infected with specified AAVs (B shows imaging plane). Representative images of tdT-only control group (left; n = 4) and UNC5C misexpression group (right, n = 5). Lower dendrite density in UNC5C group is not explained by a difference in number of infected starburst cells (Supplemental Fig. S7A).

D-F. Representative cross-sections showing IPL projections of starburst (magenta, anti-tdTomato; white, anti-ChAT) and Hb9-ooDSGC (green, anti-GFP) dendrites in retinas infected with specified AAVs. Laminar targeting is normal in retinas expressing tdTomato alone (D; n = 4 mice), but is disrupted by Chat-UNC5C misexpression (E, Hb9-DSGCs, n = 4 mice; F, starbursts, n = 5 mice).

G,H. Working model for FLRT2-UNC5C function. During normal development (G), FLRT2$^+$ DS circuit dendrites branch exuberantly as they grow. Properly stratified branches are stabilized by FLRT-LPHN adhesion (+). Branches that stray into adjacent IPL layers contact UNC5$^+$ amacrine arbors; this blocks FLRT-LPHN adhesion leading to branch elimination (X). Upon Chat-UNC5C misexpression (H), correctly targeted arbors in S2 receive a large UNC5 signal (large X), thereby diminishing FLRT2-LPHN adhesion and suppressing growth. Ectopic UNC5 signal may be larger than endogenous UNC5 signal (small X). Survival and growth of mistargeted arbors indicates that neurons compare relative levels of UNC5 signaling – and hence relative levels of FLRT2-LPHN positive signals – across their dendritic branches to determine which branches will survive.
Scale bars, 20 μm. Bar in D applies to E,F. Also see Supplemental Fig. S7.

Key resources table

REAGENT or RESOURCE	SOURCE	IDENTIFIER
Antibodies		
guinea pig anti-bassoon	Synaptic Systems	RRID:AB_2290619; Cat# 141004
goat anti-ChAT	Millipore	RRID:AB_2079751; Cat# (AB144P
rabbit anti-FLRT2 (Western blot)	Thermo	Cat# PA5–109729
goat anti-FLRT2 (immunostaining)	R&D Systems	RRID:AB_2106600; Cat# AF2877
mouse anti-GAD65 clone GAD6	EMD Millipore	RRID:AB_2263126; Cat# (MAB351
mouse anti-gephyrin clone mAb7a	Synaptic Systems	RRID:AB_2232546; Cat# 147021
rabbit anti-GFP	Millipore	RRID:AB_2630379; Cat# AB3080P
goat anti-GFP	Abcam	RRID:AB_304897; Cat# ab5450
rat anti-Neurofilament-M clone 2H3	Developmental Studies Hybridoma Bank	RRID:AB_531793; Cat# 2H3
rabbit anti-Satb1/2 clone EPR3951	Epitomics/ Abcam	RRID:AB_10862207; Cat# ab109122
guinea pig anti-VAChT	Millipore	RRID:AB_2187981; Cat# AB1588
mouse anti-Flag clone M2	Sigma	RRID:AB_262044; Cat# F1804
mouse anti-LPHN3	Santa Cruz (ref [88])	Cat# sc-393576
rabbit anti-UNC5C	NSJ	Cat# R31843
rat anti-hemagglutinin (HA)	Sigma	RRID:AB_390915; Cat# 11867423001
rabbit anti-mCherry (detects tdTomato)	Kerafast	Cat# EMU106
donkey anti-rabbit Alexa-488	Jackson Immunoresearch	RRID:AB_2313584; Cat# 711–545-152
donkey anti-goat Cy3	Jackson Immunoresearch	RRID:AB_2307351; Cat# 705–165-147
donkey anti-guinea pig Cy3	Jackson Immunoresearch	RRID:AB_2340460; Cat# 706–165-148
donkey anti-goat Alexa-647	Jackson Immunoresearch	RRID:AB_2340437; Cat# 705–605-147
donkey anti-guinea pig Alexa-647	Jackson Immunoresearch	RRID:AB_2340476; Cat# 706–605-148
donkey anti-mouse Alexa-647	Jackson Immunoresearch	RRID:AB_2340863; Cat# 715–605-151
donkey anti-rat Alexa-647	Jackson Immunoresearch	RRID:AB_2340694; Cat# 712–605-153
Bacterial and virus strains		

REAGENT or RESOURCE	**SOURCE**	**IDENTIFIER**
AAV: PHP.eB-CAG-flex-tdTomato-WPRE-pA	Gift of Edward Boyden (MIT) via Addgene	Addgene 28306-PHPeB
AAV: PHP.eB-CMV-flex-Unc5cHA-WPRE-SV40pA	Duke Viral Vector Core; this study	n/a
Chemicals, peptides, and recombinant proteins		
Protein A/G beads for immunoprecipitation	Pierce	Cat# 88803
Critical commercial assays		
HCR probeset: *Gad2*	Molecular Instruments	Probe lot# RTA798
HCR probeset: *Unc5c*	Molecular Instruments	Probe lot# RTB893
RNAScope probeset: *Gad2*	ACD	Cat# 439371
RNAScope probeset: *Unc5c*	ACD	Cat# 403211
Deposited data		
Amacrine cell scRNA-seq	Yan et al.[42]	Broad Single Cell Portal: SCP919
Adult RGC scRNA-seq	Tran et al.[61]	Broad Single Cell Portal: SCP509
Developing RGC scRNA-seq	Shekhar et al.[74]	Broad Single Cell Portal: SCP1706
Purified retinal neuron subtypes Affymetrix microarray	Kay et al.[59]	NCBI GEO: GSE35077
Experimental models: Cell lines		
HEK 293	ATCC	RRID:CVCL_0045; Cat#CRL-1573
Experimental models: Organisms/strains		
mouse: $\mathit{Unc5c}^{\mathit{rcmTg(Ucp)1.23Kz}}$ (*Unc5c* null)	Gift of Susan Ackerman (UCSD), see Ackerman et al.[48]	MGI:1857852
mouse: $\mathit{Unc5d}^{\mathit{tm1Kln}}$ (*Unc5d* null)	Gift of Viktor Tarabykin (Charité, Berlin), see Yamagishi et al.[35]	MGI:5495472

REAGENT or RESOURCE	SOURCE	IDENTIFIER
mouse: *Flrt2*$^{tm1c(EUCOMM)Wtsi}$/*RobH* (*Flrt2*^{flox})	EMMA repository	MGI:6119416
mouse: *Tg(Six3-cre)69Frty*	Jackson labs	RRID:IMSR_JAX: 019755
mouse: *Tg(Drd4-EGFP)W18Gsat*	Gift of Joshua Sanes (Harvard)	RRID:MMRRC_000231-UNC
mouse: *B6.Cg-Tg (Hlxb9-GFP)1Tmj/J* (Hb9-GFP)	Jackson labs	RRID:IMSR_JAX:005029
mouse: *Chat*$^{tm2(cre)Lowl}$	Jackson labs	RRID:IMSR_JAX:006410
mouse: *Slc17a6*$^{tm2(cre)Lowl}$/J (Vglut2^{Cre})	Jackson labs	RRID:IMSR_JAX:016963
mouse: *Flrt2*^{UF}	This study	Jackson labs stock #038570
mouse: CD-1	Charles River	RRID:IMSR_CRL:022
mouse: C57Bl6/J	Jackson labs	RRID:IMSR_JAX:000664
mouse: SJL/J	Jackson labs	RRID:IMSR_JAX:000686
mouse: B6SJLF1/J	Jackson labs	RRID:IMSR_JAX:100012
Oligonucleotides		
Flrt2^{UF} genotyping-outer F	IDT	TGGATGAGTTCCCCATGAACCTTC
Flrt2^{UF} genotyping-outer R	IDT	GAGATGATCGAAGACTCCTTGAGTTAACATTCGT
Flrt2^{UF} genotyping-inner F	IDT	GCGATTAGCCTCAAACTGTTGTTTTTATCGAAGAATAAT
Flrt2^{UF} genotyping-inner R	IDT	CAACAGGCACGCTACTCAGGTG
Flrt2^{UF} founder screening 1st PCR F	IDT	accgcggtggcggcc GCT CCT CAA GCT GGA AGA ACT CCA
Flrt2^{UF} founder screening 1st PCR R	IDT	tagaggatccactag TGT CTG ATA TGA CGG CAA TTC GGT
Flrt2^{UF} founder screening cloned fragment PCR F	IDT	caaggcgattaagttgggtaac
Flrt2^{UF} founder screening cloned fragment PCR R	IDT	gcgtgttcgaattcgccaatgac
sgRNA for generating *Flrt2*^{UF} genomic mutation (DNA template sequence)	This study	GCCCAACAGGCACGCTACTCagg
Repair oligo for generating *Flrt2*^{UF} genomic mutation	IDT	gctcctcaagctggaagaactccacctggacgacaactccatatctacagtgggagtagaagacggagcgttccgggaagcgattagcctcaaactgttgtttttatcgaagaataatctgagt
Recombinant DNA		
plasmid: pAAV-CMV-flex-Unc5cHA-WPRE-SV40pA	This study	Addgene 205442

REAGENT or RESOURCE	SOURCE	IDENTIFIER
plasmid: pCMV-Lphn3-GFP	Gift of Matthew O'Sullivan (Duke), see O'Sullivan et al.[34]	n/a
plasmid: pTT3-Unc5c^{WT}-flag	Gift of Woj Wojtowicz (Stanford), see Visser et al.[30]	Addgene 72196
plasmid: pTT3-Unc5c^{UF}-flag	This study	n/a
Software and algorithms		
R version 4.1.2	https://cran.r-project.org/	RRID:SCR_001905
FIJI	Schindelin et al.[85]	RRID:SCR_002285
Seurat version 4.0	Stuart et al.[87]	RRID:SCR_007322
P5 RGC scRNAseq online viewer	Rheaume et al.[60]	https://health.uconn.edu/neuroregeneration-lab/rgc-subtypes-gene-browser/
Puncta Analyzer	Ippolito and Eroglu, 2010[82]; Savage et al. 2023[83].	dx.doi.org/10.17504/protocols.io.3byl4qewjvo5/v1
Object Finder	Della Santina et al.[51]	https://zenodo.org/record/4767847